NTNU – Trondheim
Norwegian University of
Science and Technology

Ice-Induced Loading on Ship Hull During Ramming

Ørjan Fredriksen

Marine Technology
Submission date: June 2012
Supervisor: Bernt Johan Leira, IMT
Co-supervisor: Professor Jørgen Amdahl, IMT

Norwegian University of Science and Technology
Department of Marine Technology

NTNU
Norwegian University of Science and Technology
Department of Marine Technology

Master Thesis, Spring 2012
for
Stud. Techn. Ørjan Fredriksen

Ice-Induced Loading on Ship Hull During Ramming

Belastning på Skipsskrog ved Is-bryting

Transport and exploitation of resources in the Northern areas are increasingly focused upon. The corresponding climatic conditions represent a challenge both to the operation and design of ships in these waters.

The presence of sea ice is the main factor hindering operations in Arctic. Sea ice is a complex material and induces high pressures when being in contact with ships or structures. To understand the nature of the associated forces, the ice physics and ice mechanics have to be studied.

For ice-breaking vessels significant forces will be acting on the hull during the ramming process. The possibility of dynamic amplification of the hull response is also relevant. This is to be considered in more detail in the present thesis with main focus on numerical response calculations.

As the result of a project which was managed by DnV, *Ice Load and Monitoring (*ILM), which was supported by the Norwegian Research Council, a large amount of measurements from the coast-guard vessel Svalbard was obtained. These data also comprise ramming events, and it may be relevant to apply these in order to make comparison with results from numerical calculations.

The following subjects are to be examined:

1) Different types of sea ice and their mechanical/physical properties are to be described. Furthermore, models for evaluation of ice-ship interaction (calculation of contact pressure acting on a structure due to ice) are to be presented and discussed together with relevant input parameters to these models. This includes local ice pressure acting on the hull and global loads due to ramming etc.

2) A brief review of ice classes for ships is performed with focus on DNV and IACS unified rules for Polar Ships. In particular, the classes which correspond to vessels which are intended for ice-breaking purposes are to be addressed.

3) Methods for computation of hull response during ramming are to be reviewed and summarized. A beam element model of the hull girder is subsequently to be established for the vessel KV Svalbard e.g. by application of the computer program Abaqus. The natural frequencies are identified based on this model, and transient dynamic response due to ramming is to be computed.

4) Parameter variations are to be performed in relation to the calculations which are performed in em 3. This applies e.g. to the structural beam modeling and the representation of the loading.

The methodology and parameters associated with the numerical time integration can also be considered.

5) A more detailed model of the hull based on application of shell elements is to be established. To the extent that time allows, parameter studies are also to be performed for this hull model e.g. in relation to different meshes and different load representations in space and time. Comparison is to be made between response computed from the beam versus the shell model. Evaluation of the model based on recorded motions of KV Svalbard during ramming of ice may also be considered.

The work scope may prove to be larger than initially anticipated. Subject to approval from the supervisor, topics may be deleted from the list above or reduced in extent.

In the thesis the candidate shall present his personal contribution to the resolution of problems within the scope of the thesis work.
Theories and conclusions should be based on mathematical derivations and/or logic reasoning identifying the various steps in the deduction.

The candidate should utilise the existing possibilities for obtaining relevant literature.

The thesis should be organised in a rational manner to give a clear exposition of results, assessments, and conclusions. The text should be brief and to the point, with a clear language. Telegraphic language should be avoided.

The thesis shall contain the following elements: A text defining the scope, preface, list of contents, summary, main body of thesis, conclusions with recommendations for further work, list of symbols and acronyms, references and (optional) appendices. All figures, tables and equations shall be numbered.

The supervisor may require that the candidate, in an early stage of the work, presents a written plan for the completion of the work. The plan should include a budget for the use of computer and laboratory resources which will be charged to the department. Overruns shall be reported to the supervisor.

The original contribution of the candidate and material taken from other sources shall be clearly defined. Work from other sources shall be properly referenced using an acknowledged referencing system.

The thesis shall be submitted in 3 copies:

- Signed by the candidate
- The text defining the scope included
- In bound volume(s)
- Drawings and/or computer prints which cannot be bound should be organised in a separate folder.

Supervisors: Professor Bernt J. Leira /Professor Jørgen Amdahl

Contact person at DNV: Håvard Nyseth

Deadline: June 6th 2012

Trondheim, January 16th, 2012

Bernt J. Leira

Preface

The following report is an individual master's thesis in the field of marine structural engineering undertaken during the spring semester of 2012. The thesis work has mainly been carried out at the Department of Marine Technology, Norwegian University of Science and Technology in Trondheim with the exception of one month's work at the headquarters of Det Norske Veritas, Høvik.

Throughout the semester, more time than anticipated has been devoted to establishing a global finite element model using software Patran-Pre, which I have previously not used. Further, development of scripts and routines in MATLAB for serial finite element analyses and post-processing of output data has demanded more time than first expected.

The work has been a highly educational experience, where I have had the opportunity to put theoretical knowledge from different fields of marine engineering into practice for problems of high relevance in today's maritime industry. I have also had the chance to gain experience using different software packages that are widely adapted in the engineering industry.

I wish to extend my gratitude towards thesis advisors Professor Bernt Johan Leira and Professor Jørgen Amdahl for their helpful guidance and discussions. Further, I would like to thank Håvard Nyseth at Det Norske Veritas for his appreciated input on many occasions, and for the opportunity to attend and experience a full scale ice trial in the Bay of Bothnia. Finally, Martin Storheim at the Department of Marine Technology deserves recognition for his help regarding finite element modelling.

Ørjan Fredriksen
Trondheim, June 2012

Abstract

As a result of the steadily increasing activities related to marine technology in Arctic regions, Det Norske Veritas has launched an ice load monitoring project to gather knowledge of the ice conditions and prevailing ice-induced actions in the region. The intention of the following thesis is to study different aspects related to design of ice-going vessels, in particular the design scenario where a vessel impacts an ice ridge.

The introductory part of the thesis gives an overview of important aspects related to sea ice, including different types of ice features and their physical and mechanical properties. The microstructure of pure ice and formation mechanisms of sea ice are briefly described, and mechanical properties such as elasticity and compressive strength are discussed. Further, a study of existing models for estimation of ice-induced loading on ships is carried out, with focus on local hull plating pressure and global loading due to ice ridge impact.

A comparative study of design rules developed by Det Norske Veritas and the International Association of Classification Societies is conducted, and important differences between the two separate rules are identified. The subdivision of class notations is described, and differences in definition of design loads and corresponding requirements are presented. A general conclusion is that the rules developed by Det Norske Veritas are more specific when it comes to governing design scenarios, while rules set forth by the International Association of Classification Societies are more universal in terms of vessel type and prevailing ice conditions.

Two separate finite element models based on coastguard vessel KV Svalbard are developed, including a simplified beam element model and a detailed shell element model. Quasi-static and dynamic response analyses for ice ridge impact loading are carried out, where the duration of the load pulse is varied systematically from 0.25 s to 2.0 s. The simplified finite element model is seen to give larger overall maximum response compared with the detailed model, but the difference decreases as the pulse duration is increased.

It is observed that quasi-static response is overall larger than dynamic response for both finite element models within the defined pulse duration range. However, the ratio of maximum dynamic to maximum quasi-static response is seen to be posi-

tively correlated with the load pulse duration, and a linear relationship is observed.

A study of different parameter variations is performed in order to investigate the importance of various pulse shapes, mass models, damping models and solution methods. Variations are only performed using the simplified beam model. It can be concluded that the shape of the load pulse is of minor importance for dynamic response when the pulse duration is short. However, the pulse shape becomes increasingly important for longer load pulses.

An opposite trend is observed when varying the mass model, where a negligible difference in dynamic response is seen for longer load pulses. The difference increases somewhat for shorter load pulses, but can be considered unimportant for dynamic response within the investigated duration interval.

It is further observed that the choice of damping model is of significant importance compared with other investigated parameters, and the difference in predicted response remains constant within the investigated pulse duration interval. The choice of solution method is however unimportant for analysis using the simplified beam model.

In order to verify the applicability of the finite element models, full scale sea trial measurements of global motions from KV Svalbard are analysed and compared with finite element results. Difference between measured and calculated response during ice ridge impact is seen to be significant, where the calculated maximum response is close to 4 times larger than the maximum measured response. Iterative modifications of the load pulse shape are performed in order to reproduce the measured response history following ice ridge impact, and quite strong agreement is obtained between measured and calculated response.

Sammendrag
(Norwegian Abstract)

Som et resultat av stadig økende aktiviteter knyttet til marin teknologi i arktiske strøk, har Det Norske Veritas lansert et prosjekt knyttet til overvåkning av islaster for å samle kunnskap om isforhold i denne regionen. Intensjonen bak følgende rapport er å studere ulike aspekter knyttet til design av isgående fartøy, spesielt tilfellet hvor det oppstår sammenstøt mellom fartøy og skrugard.

Den innledende delen av rapporten gir et innblikk i viktige forhold knyttet til havis, deriblant fysiske og mekaniske egenskaper. Mikrostrukturen til is, samt mekanismene bak dannelse av havis er beskrevet, og mekaniske egenskaper som elastisitet og trykkfasthet presenteres. Videre er det utført en studie rundt eksisterende modeller for estimering av is-indusert belastning på skip, med fokus på lokalt skrogplatetrykk og global belastning fra sammenstøt med skrugard.

Det er videre gjort en sammenlikning av gjeldende regelverk utviklet av Det Norske Veritas og International Association of Classification Societies der hvor viktige forskjeller identifiseres. Strukturen for inndeling av klassenotasjoner er beskrevet, og forskjeller i definisjon av dimensjonerende belastning presenteres. En generell konklusjon er at regelverket til Det Norske Veritas er mer spesifikt når det gjelder definisjon av designbelastning, mens regler fastsatt av International Association of Classification Societies er mer generelle i form av fartøytype og isforhold.

To separate elementmodeller basert på kystvaktfartøyet Svalbard er utviklet, deriblant en forenklet bjelkemodell og en mer detaljert skallmodell. Kvasi-statiske og dynamiske responsanalyser for belastning fra sammenstøt med skrugard er utført, hvor varigheten av belastningen er systematisk variert mellom 0.25 s og 2.0 s. Den forenklede bjelkemodellen gir generelt større maksimal respons sammenlignet med den detaljerte skallmodellen, men forskjellen minker når lastpulsens varighet øker.

Det er observert at kvasi-statisk respons generelt er større enn dynamisk respons for begge elementmodeller innenfor det definerte varighetsområdet for lastpuls. Imidlertid er forholdet mellom maksimal dynamisk og maksimal kvasi-statisk respons positivt korrelert med lastpulsens varighet, og en tilnærmet lineær sammenheng er observert.

Videre utføres en rekke parametervariasjoner for å undersøke betydningen av ulike

pulsformer, massemodeller, dempningsmodeller og løsningsmetoder. Parameterstudiet utføres bare med den forenklede bjelkemodellen. Det kan konkluderes med at formen på lastpulsen er av mindre betydning for dynamisk respons ved kort pulsvarighet. Imidlertid blir pulsformen viktigere ved lengre lastpulser.

En motsatt trend er observert ved endring av massemodell, hvor forskjell i dynamisk respons er ubetydelig ved lengre pulsvarighet. Forskjellen øker noe for kortere lastpulser, men kan betraktes som uvesentlig for dynamisk respons innenfor det definerte varighetsområdet.

Det er videre observert at valg av dempningsmodell er av vesentlig betydning sammenlignet med andre undersøkte parametere, der forskjellen i dynamisk respons forblir konstant innenfor det definerte varighetsområdet. Valget av løsningsmetode er imidlertid uvesentlig for analyser med den forenklede bjelkemodellen.

For å verifisere anvendelse av elementmodellene, er fullskala målinger av globale bevegelser fra KV Svalbard analysert og sammenlignet med resultater fra modellene. Forskjell mellom målt og beregnet respons anses å være betydelig, hvor beregnet maksimal respons er tilnærmet fire ganger større enn maksimal målt respons. Iterative modifikasjoner av lastens pulsform er utført for å reprodusere den målte responshistorien, og det er oppnådd godt samsvar mellom målt og beregnet respons.

Contents

List of Figures

List of Tables

List of Symbols

α	Mass-proportional Rayleigh coefficient
β	Stiffness-proportional Rayleigh coefficient
Δ	Vessel mass displacement
$\dot{\epsilon}$	Strain rate
$\dot{\sigma}$	Stress rate
η	Sea ice porosity
η_3	Heave displacement
η_5	Pitch angle
η_b	Brine volume fraction
η_j	Displacement in j direction
ω_i , ω_j	Circular oscillation frequency
$\overline{C}$	Damping matrix
$\overline{K}$	Stiffness matrix
$\overline{M}$	Inertia matrix
ρ	Mass density of sea water
σ	Normal stress
τ	Shear stress
φ	Angle of internal friction
φ_s	Stem inclination angle
ζ_i , ζ_j	Critical damping ratio
A	Load patch area
A_{33}^{2D}	Two-dimensional heave added mass coefficient

A_{ij}	Hydrodynamic added mass coefficient
A_{wp}	Vessel waterplane area
B	Vessel breadth
C	Cohesion
C_{33}	Hydrostatic heave stiffness
C_{ij}	Hydrostatic stiffness coefficient
D	Vessel draught
d	Grain size
$F(t)$	Load-time history
F_i	Force in i direction
F_n	Normal component of ice ramming force
h_c	Load height
h_i	Ice thickness
I	Load impulse
L	Load length
M_{total}	Total mass of vessel including hydrodynamic mass
p_{ave}	Average ice pressure
p_c	Ice pressure
R^2	Coefficient of determination
R_F	Flexural strength of sea ice
R_H	Horizontal compressive strength of sea ice
R_V	Vertical compressive strength of sea ice
S_3	Vertical displacement
T	Temperature
t_1	Load pulse duration
T_3	Natural heave oscillation period
v_{ship}	Vessel ramming speed
X	Distance from COG to bow
ABL	Above Base Line
ASCII	American Standard Code for Information Interchange

CAE	Computer-Aided Engineering
COG	Centre of Gravity
DLF	Dynamic Load Factor
DNV	Det Norske Veritas
FE	Finite Element
FFT	Fast Fourier Transform
FP	Forward Perpendicular
GMT	Greenwich Mean Time
GPS	Global Positioning System
IACS	International Association of Classification Societies
IGES	Initial Graphics Exchange Specification
ILM	Ice Load Monitoring
KV	Kystvakt
MRU	Motion Reference Unit
NTNU	Norges Teknisk-Naturvitenskapelige Universitet
UIWL	Upper Ice Waterline
USCG	United States Coast Guard
WMO	World Meteorological Organization

Chapter 1

Introduction

In recent years, activities related to the exploitation of offshore oil and gas resources in Arctic areas have seen a tremendous increase. Parallel to this development, a rapidly expanding maritime transport industry is continuously pursuing more efficient trading routes between Europe and Eastern Asia. The presence of sea ice proposes new and demanding challenges related to the execution of marine operations in Arctic areas.

The challenges associated with operations in ice-infested waters have established a permanent need for proper rules and guidelines to serve as a benchmark for the level of quality required when designing marine structures for Arctic conditions. At present, calculation of ice-induced actions on ships is mainly based on empirical methods due to the lack of a unified theory that is able to properly explain the underlying physical mechanisms.

As a response, Det Norske Veritas initiated an *ice load monitoring* project in order to gain a better physical understanding of the ice conditions and prevailing ice-induced actions experienced by vessels in Arctic areas. The ongoing project has included full scale sea trials with coastguard vessel and icebreaker KV Svalbard during the winters of 2006, 2007, 2011 and 2012. These sea trials have provided vast amounts of valuable data, including strain measurements in the bow region of the vessel and measurements of global motions during ice ridge ramming.

The intention of this thesis is to study global vessel response during ramming of ice ridges, which is considered a design load scenario for ice-going vessels. Different aspects of sea ice are first studied, along with a review of current ice class rules and an overview of important ship-ice interaction models. Further, two separate global finite element models are developed based on the main particulars of the vessel KV Svalbard. Dynamic response analyses are carried out using these models to obtain time histories of global vessel motions during ice ramming. In order to verify the results, full scale measurement data from the aforementioned sea trial in 2012 are analysed and compared with the finite element calculations.

Chapter 2

Different Aspects of Sea Ice

2.1 Types of Sea Ice

In ice-infested waters, sea ice can appear in many different forms. Depending on the type of marine structure to be designed, different ice features may be of importance. Sea ice can be categorized according to stage of development, ice feature size and type of surface feature. Further, it is distinguished between fast ice and floating ice. In the following, a brief introduction to the different sea ice features and the associated nomenclature will be given along with an overview of how ice features are classified.

2.1.1 Developmental Stages of Sea Ice

A common method of classifying sea ice features is by considering the stage of development of the ice. According to [WMO, 1970], the development of an ice cover can be separated into six different stages, namely *new ice*, *nilas*, *pancake ice*, *young ice*, *first-year ice* and *old ice*. Recently formed ice is naturally categorized as new ice and will undergo several intermediate stages before entering the next developmental stage. The different intermediate stages are summarized in table 2.1.

Intermediate stage	Description
Frazil ice	Platelets of pure ice crystals that have just been formed
Grease ice	Later stage of freezing in which platelets freeze together
Slush	Snow mixed together with sea water on an ice surface
Shuga	Spongy white ice lumps formed from grease ice or slush

Table 2.1: Intermediate stages of new ice

As ice enters the nilas stage, a thin crust has been formed with a thickness less than 10 cm. Nilas ice is elastic and will easily bend when exposed to surface elevation from waves and swell sea. Depending on the thickness, nilas is usually grouped into dark nilas (thickness < 5 cm) and light nilas (thickness > 5 cm). Eventually, nilas ice will separate into smaller pieces and strike against one another, causing formation of circular *pancake ice* with raised rims around the circumference and a diameter in the range 0.3-3 m. Pancake ice may form prior to the nilas stage from slush or shuga, or after the nilas stage depending on environmental actions. The photography in figure 2.1 shows pancake ice in the Bay of Bothnia, encountered during a sea trial attended by the author in 2012.

Figure 2.1: Pancake ice in the Bay of Bothnia

Ice that exists in the transition stage between nilas and first-year ice is known as young ice. The thickness of young ice will typically be in the range 0.1-0.3 m. As young ice continues to grow throughout the winter, it will eventually develop into first-year ice with a thickness of up to 2 m. If the first-year ice survives the following summer without melting away, it is classified as old or multi-year ice. Old ice is characterized by having smoother topographic features than young ice and first-year ice due to weathering. A collective term for ice features of different stages of development that have frozen together is *ice breccia*.

2.1.2 Size of Sea Ice Features

It is mainly floating ice features that need to be categorized according to size. As previously mentioned, pancake ice characterizes small circular pieces of floating

ice with a diameter of up to 3 m. Further, any relatively flat piece of ice with a diameter of less than 20 m is known as an *ice cake*. As the size increases beyond this, the term *floe* is used to describe the ice feature. Floes can have diameters of more than 10 km, and so-called *floebergs* may protrude up to 5 m above sea level.

An *iceberg* is a massive piece of ice protruding more than 5 m above sea level which has broken away from a glacier. Icebergs can be either floating or grounded to the sea bottom. If the iceberg height is less than 5 m, it is called a *bergy bit*, and if it protrudes less than 1 m above sea level, it is characterized as a *growler*.

When it comes to fast ice, it is usually attached to shore or to the sea bottom. Coastal ice can extend up to 200 m from the coastline where it is attached, and is usually formed by nilas and young ice. *Anchor ice* is a term describing fast ice attached to the sea bottom with the top usually submerged below the waterline.

2.1.3 Different Surface Features of Sea Ice

Level ice is a general term describing sea ice which is unaffected by deformation. Several types of ice features have been exposed to forces resulting in a deformed surface shape. *Rafted ice* is formed when one ice cover overrides another, creating an elevation in the level ice. However, the most important ice-surface features in design of marine structures are *pressure ridges*.

A pressure ridge is a wall of broken ice which has been forced upwards by the pressure from the surrounding ice cover. The part of a ridge above the waterline is termed the *sail*, and the submerged part, known as the *keel*, may have a depth of up to 20 m. Usually, the keel is 4-5 times thicker than the sail, making it difficult to notice a pressure ridge in otherwise level ice. In addition, as the ridge ages, its edges will become more rounded, resulting in a well-camouflaged hazard for ships going in ice-infested waters.

A ridge that is grounded to the sea bottom is termed a *stamukha*. These features will accumulate in height as they cannot expand downwards, and may thus be easier to notice. If the ice cover is forced upwards from different directions to form a hill-shaped feature, it is classified as a *hummock*. Hummocks are basically the same features as ridges, except they do not extend like a wall along the ice cover.

2.2 Ice Physics

In order to understand the formation of different ice features and the mechanical behaviour of ice, an introduction to the physics of ice is helpful. Therefore, a presentation of the microstructure and composition of sea ice will be given with reference to [Løset et al., 2006].

2.2.1 Ice Microstructure

The microstructure of ice is composed of water molecules (H_2O) in a lattice. When the temperature of liquid water is brought below 0°C, the water molecules form a crystalline solid structure of atoms held together by hydrogen bonds. Ice can exist in at least nine crystalline forms. However, eight of these will only occur when the ambient temperature is below −80°C. This means that ice virtually has only one possible crystalline form under normal conditions. While the water molecules of the eight unattainable crystalline forms are all arranged with cubic symmetry, the naturally occurring crystal arrangement is hexagonal. For this reason, normal ice is referred to as hexagonal ice, or *ice Ih*.

The microstructure of ice has some important effects on the properties of ice as a material. First of all, the hexagonal atomic structure of ice results in a relatively open lattice. When ice melts, the atoms are brought closer together, thus causing the mass density to increase. This difference in density between water and ice causes ice to float on top of liquid water. Also, as the ice is melting, only part of the hydrogen bonds between the atoms will melt at 0°C. This means that solid ice can exist at temperatures above 0°C, causing water to have its maximum density at 4°C. This is known as the *density anomaly of water* [Furnes, 2011].

2.2.2 Sea Ice Composition

When considering the formation of sea ice, one has to take into account the salt content of sea water. As the temperature of sea water reaches 0°C, crystal-like platelets of fresh ice are formed. This causes the salinity of the surrounding water to increase as the salt is excluded from the formation process. Such ice crystals continue to form, causing the development of a slush-like oily solution with high salinity called *grease ice*. If the temperature is kept low, the ice platelets will grow thicker and attach together, forming ice of a more solid character. During this process, the surrounding saline water is trapped in brine cells within the ice structure.

As the ice mass continues to grow, further crystallization causes a reduction in the size of the brine cells, resulting in an even higher salinity of the remaining brine. Over time, drainage of brine along tubes and channels inside the ice structure will occur, creating pores within the bulk material.

The above discussion suggests that the properties of sea ice as a material depends on several parameters. The most important parameters include ambient temperature, salinity and density. Due to brine entrapment and drainage within the ice structure, ice porosity is another parameter of importance. Further, being a crystalline material, grain size and orientation of the ice crystals will also play a role in defining the mechanical properties of sea ice.

2.3 Ice Mechanics

In the following, a discussion on the main aspects of sea ice mechanics is presented. The principal source of information is [Løset et al., 2006], but other works will be cited when relevant.

2.3.1 Continuum Mechanics of Ice

From a mechanical point of view, ice exhibits similar material behaviour to that of well-known metals such as steel. This includes both ductile and brittle material behaviour followed by failure. There are however several factors that create a distinction between ice and common metals.

First of all, the grain size of ice is relatively large compared to for instance steel, thus making it more difficult to treat in the same manner. Further, ice exists very close to its melting temperature under normal circumstances, which also increases the complexity of the material behaviour.

Another complicating factor is that sea ice is a multi-phase material composed of pure ice crystals, brine cells, air pockets and solid salts. In order to fully describe the material behaviour of sea ice, one consequently has to consider both the solid and the fluid material behaviour. The first case refers to a time-independent relationship between load and displacement, while the latter means a time-dependency as the loading is a function of the fluid velocity rather than the displacement. A complete model for sea ice therefore requires a non-linear elastic model to describe the solid material behaviour, as well as visco-elastic and visco-plastic models to capture the fluid material behaviour.

Simplified Material Model

Due to the complexity of the complete material model for sea ice, simplifications are usually made without significantly affecting the result. A common simplification is to neglect all time-dependent terms and only consider the short-term loading and material behaviour. This is justified by considering that the load is applied relatively fast, which results in the time-dependent terms not having the necessary time to develop, and they may thus be neglected.

By employing this model, only the elastic-plastic behaviour is considered. In such a model, the material undergoes three different stages prior to failure, including elastic deformation until yielding, plastic strain hardening post-yielding and finally softening as the load peak is surpassed. The different stages of material behaviour are illustrated in figure 2.2.

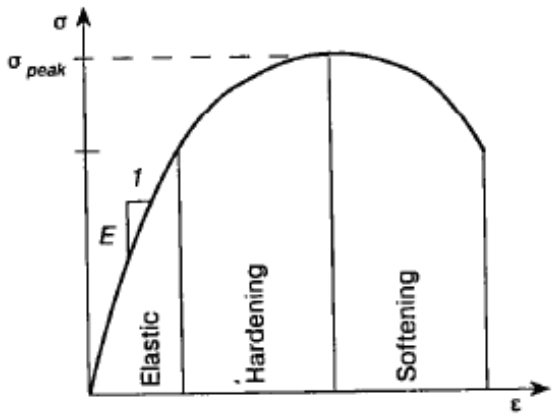

Figure 2.2: Elastic-plastic material model [Løset et al., 2006]

Coulomb–Mohr Failure Criterion

From the elastic-plastic model, material behaviour prior to failure is described. However, when determining ice-induced actions on marine structures, one is interested in the strength of sea ice since this is the maximum action exerted on the structure. For materials such as steel, the *Von Mises* or *Tresca* failure criteria are frequently applied as they require only one material parameter to determine whether the material will fail or not. On the other hand, such failure criteria require that the tensile and compressive strengths are equal, a statement which is not true for sea ice. Therefore, the *Coulomb–Mohr* failure criterion can be utilized, which is expressed by equation (2.1). This criterion explains failure as a critical combination of shear and normal stresses on a plane.

$$\tau \leq C + \sigma \tan \varphi \tag{2.1}$$

In equation (2.1), τ and σ express the shear and normal stresses on a plane, while C and φ describe the cohesion and the angle of internal friction, as defined in figure 2.3. In the case of materials with equal tensile and compressive strengths, the angle of internal friction equals $\pm 45°$ and the Coulomb–Mohr criterion can be replaced by the Tresca criterion.

2.3.2 Mechanical Properties of Sea Ice

As previously indicated, the mechanical behaviour of sea ice depends on several parameters. These can be categorized as being either *state variables*, such as the ambient temperature and the loading rate, or characterizing the *type of material*, such as the grain size and porosity of the ice. The mechanical properties of sea

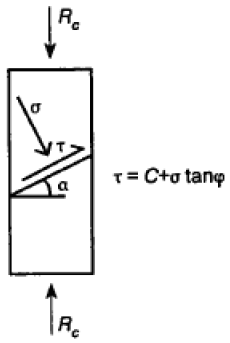

Figure 2.3: Coulomb–Mohr failure criterion [Løset et al., 2006]

ice are not constant values, but rather functions of the state variables and the type of material. Further, the state variables can have an effect on the parameters describing the type of material, such as the fact that ambient temperature and salinity govern the porosity of ice.

However, the most important parameters affecting the mechanical properties of sea ice are temperature T, porosity η, grain size d and loading rate $\dot{\sigma}$ or $\dot{\epsilon}$. In general, for increasing T, η and d, sea ice becomes weaker and softer as a material. This means that both strength and elasticity is lowered as these parameters increase. On the other hand, as the loading rate is increased, the strength of sea ice also increases until the material undergoes brittle failure due to the development of cracks. This process is however governed by the fracture mechanics of sea ice, which will not be further addressed.

Elastic Stiffness Properties

Several experiments have been carried out with the intention of determining the elastic properties of sea ice. Due to the complex material behaviour of ice, elastic properties can be difficult to measure. However, [Kamarainen, 1993] suggests that the Young's modulus of sea ice has a value in the range of 4-6 GPa. Also, a Poisson's ratio of 0.3 is suggested.

Strength Properties

As previously stated, the strength of sea ice depends on whether the loading is tensile or compressive. In general, sea ice is anisotropic, meaning that the strength also varies with the loading direction. It is often assumed that sea ice is orthotropic due to the physical mechanisms governing its growth. Since growth takes place in the vertical direction, parallel to the direction of heat flow between water below the ice and air above, crystals align vertically within the so-called *columnar zone* of the

ice. The result is stronger ice in the vertical direction compared to the horizontal direction.

It is evident that the strength of sea ice must be characterized both in terms of whether the loading is tensile or compressive, and whether the loading is applied in the horizontal or vertical direction. [Timco and Frederking, 1990] performed uniaxial compression tests on sea ice and found that the vertical strength was approximately three times the horizontal strength with values in the range 5-15 MPa and 2-5 MPa, respectively. The following approximate formulas were developed for porosities $\eta \leq 0.2$.

$$\begin{aligned} R_V &= 160\,(\dot{\epsilon})^{0.22}\left[1-\sqrt{\tfrac{\eta}{0.2}}\right] \\ R_H &= 37\,(\dot{\epsilon})^{0.22}\left[1-\sqrt{\tfrac{\eta}{0.27}}\right] \end{aligned} \tag{2.2}$$

In equation set (2.2), R_V and R_H represent the vertical and horizontal compressive strengths of sea ice, while $\dot{\epsilon}$ and η express the strain rate and porosity.

According to classical beam theory, the tensile strength of a material should be equal to its flexural strength, meaning that the maximum bending stress is the same as the maximum axial stress. This assumption can also be applied to sea ice, but it is however distinguished between the tensile and flexural strengths because of the different measurement procedures adapted during testing. According to [Lainey and Tinawi, 1984], the uniaxial tensile strength of sea ice has been measured in the range of 0.1-2 MPa depending on parameters such as ambient temperature and porosity.

[Timco and O'Brien, 1994] have developed an empirical formula for the flexural strength of sea ice:

$$R_F = 1.76e^{-5.88\sqrt{\eta_b}} \tag{2.3}$$

In equation (2.3), the parameter $0 \leq \eta_b \leq 1$ symbolizes the brine volume fraction of sea ice.

Chapter 3

Ship-Ice Interaction Models

When designing ships intended to go in ice-infested waters, it is important to have a physical understanding of the different mechanisms related to ice-induced loading on a vessel hull. Further, one must realize that the governing ship-ice interaction scenario depends on the ice conditions encountered and the way in which the vessel is operated in these conditions.

In the following, models for evaluating ship-ice interaction will be discussed and relevant design parameters are presented. Focus will be on local ice pressure models and global ice ramming models.

3.1 Local Ice Pressure

Since ice loading is a result of the contact between an ice feature and the hull, it is commonly assumed that ice loads act as localized pressure on a *load patch*. In level ice, it is natural to expect the load patch to be narrow in the vertical direction and long in the horizontal direction. Further, the pressure within the load patch is often considered as a uniform average pressure. However, there will be uncertainty related to both the magnitude and distribution of the ice pressure within the load patch and the actual dimensions of the load patch area.

3.1.1 Load Patch Area

In reality, the contact area between ice feature and hull will be of irregular shape and virtually impossible to determine. An idealization of the load patch is therefore necessary, and for response calculations of local structural elements it is convenient to assume a rectangular load patch, as illustrated in figure 3.1. This simplification

suggests that the local ice load depends on three quantities, namely ice pressure p_c, load height h_c and load length L.

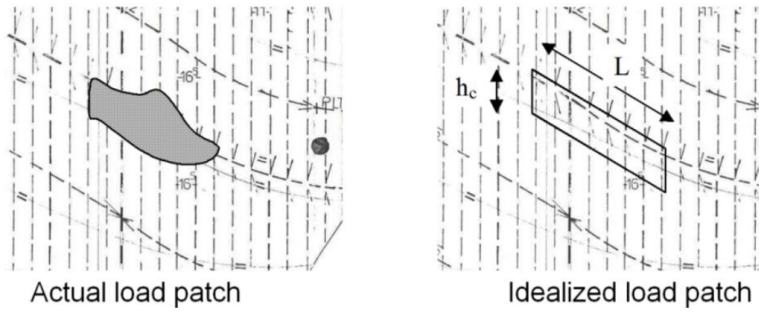

Figure 3.1: Idealization of load patch for structural design [Riska, 2011]

In structural design, the appropriate load length will depend on the type of structural element to be analysed. For vertical frames, the load length should correspond to the frame spacing, while for horizontal frames it will commonly be taken equal to the frame span. The load patch should also be placed at the location that gives rise to the largest response, meaning at midspan of frames and at centre of plate fields. Use of such simple structural idealizations is justified by the fact that the advantage of more advanced methods disappears due to the uncertainty concerning ice load values [Riska, 2011].

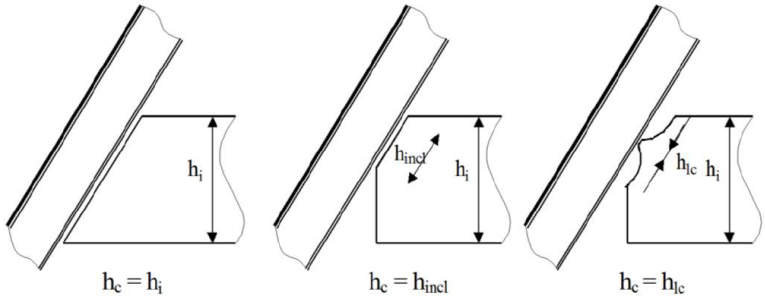

Figure 3.2: Development in definition of load patch height [Riska, 2011]

When it comes to the load height, it was initially assumed in Finnish–Swedish design rules that it should correspond roughly to the ice thickness h_i. However, this assumption proved to underestimate the loading, especially for plating in longitudinally-framed hull structures. The magnitude of the load height was decreased during the 1985 revision of the rules, as seen in figure 3.2. The line load value $q = p_c h_c$ was kept constant, meaning an increase in ice pressure. Further investigations have shown that the load height is even smaller than what is specified in the design rules, but this has so far not been taken into account.

3.1.2 Calculation of Ice Pressure

As previously discussed, ice loading is frequently modelled as a localized average pressure acting within a load patch. However, detailed observations have revealed considerable variation of local ice pressure inside the nominal contact area. There exist several models for predicting the magnitude of local ice pressure.

The original model by [Korzhavin, 1971] suggests that the ice pressure is uniform and proportional to the compressive strength of ice. The model assumes that the proportionality factor depends on the contact surface shape and *quality of contact*, while the compressive strength is a function of temperature and strain rate. However, since the compressive strength is a difficult parameter to determine and other important parameters such as the velocity are not considered, this simplified model has lost support.

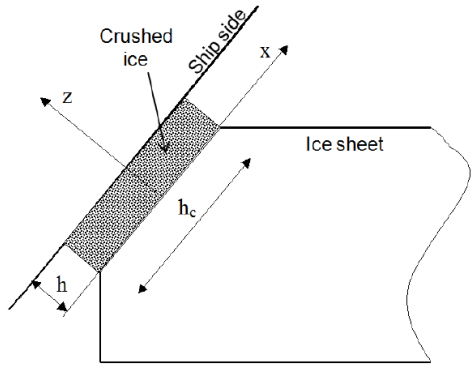

Figure 3.3: Definition of geometry for crushed ice flow [Riska, 2011]

It has been observed that the highest pressure magnitudes are obtained when the ice fails by *crushing*, that is, disintegration of the ice into small particles upon contact with the hull. As the vessel proceeds through ice, crushing creates a flow of particles away from the contact area. This flow has been analysed as a viscous fluid by, among others, [Popov et al., 1968] and a proportionality according to equation (3.1) has been established. Relevant parameters for the equation are described in figure 3.3.

$$p \propto \left[\left(\frac{h_c}{2}\right) - x^2\right]^{0.25} \tag{3.1}$$

Due to the many limiting assumptions behind the viscous fluid model, it has not been applied extensively in design. However, the physics behind the model were used in development of the Polar ice class rules by IACS.

Another important observation regarding ice pressure is that the magnitude of the average pressure is dependent on contact area size. Based on a large amount

of data, [Sanderson, 1988] suggested an upper limit for the relationship between pressure and area according to equation (3.2).

$$p_{ave} = 8.1A^{-0.57} \quad [\text{MPa}] \tag{3.2}$$

The values of the constant and the exponent in equation (3.2) have been researched extensively and found to vary considerably [Riska, 1987]. This confirms the empirical nature of the pressure-area model and the lack of physical understanding of the phenomenon. However, the pressure-area model is the most commonly applied approximation to determine the magnitude of ice pressure in design.

3.2 Global Ice Ramming

An important design scenario for a vessel in ice-infested waters is ramming of an ice ridge. Due to the large size of a typical ice ridge, it is apparent that the induced loading will affect the whole structure. Consequently, the vessel will slow down when penetrating into the ridge, thus relying on its own inertia to accomplish full ridge penetration.

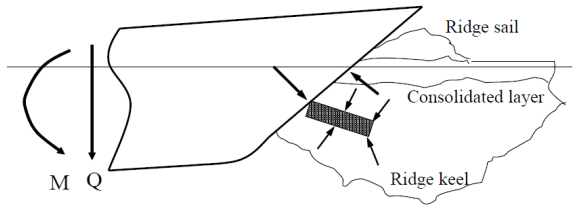

Figure 3.4: Ramming of an ice ridge [Riska, 2011]

Ice ridges are important obstacles encountered by ice-going vessels, and the global loads that arise during ramming will induce shear forces and bending moments in the hull girder that are governing for global strength design. In order to investigate vessel response due to ice ramming, it is important to understand the physics that govern the ramming problem.

3.2.1 Impact Problem

Ice ramming is an impact problem, meaning the duration of the ramming force is shorter than the natural periods of the vessel rigid body motions. The pulse-like time-variation of the force makes ice ramming a transient phenomenon and the induced vessel response will therefore decay with time. When dealing with impact problems, the most important quantity will be the maximum response

during the first oscillation of the system, as this will correspond to the largest response [Bergan et al., 1983].

Often, the load *impulse* is used as a characteristic quantity of the force-time variation. The load impulse is defined according to equation (3.3), where t_1 corresponds to the pulse duration.

$$I = \int_0^{t_1} F(t)\, dt \tag{3.3}$$

Since the load impulse is defined as the area under the force-time history curve, several different combinations of pulse shape and duration may yield the same impulse magnitude. Figure 3.5 gives an indication of the dynamic amplification in a system resulting from different combinations of pulse shape and duration.

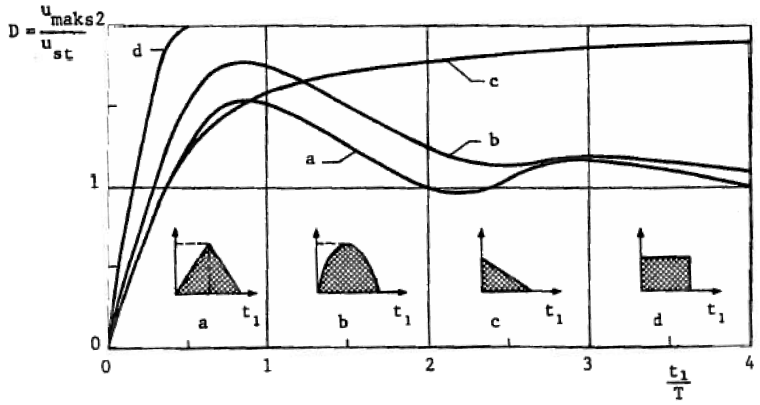

Figure 3.5: Dynamic amplification factor for different analytical force-time histories [Bergan et al., 1983]

3.2.2 Determination of Ramming Force

There have not been many attempts to describe ramming loads which are properly described in research literature. However, [Riska, 1987] analysed the ramming interaction between a ship and a massive ice floe and developed a calculation model for global ramming force. The model is valid when the ramming direction is perpendicular to the ice floe edge, meaning no oblique impacts on the side of the hull. This implies that only surge, heave and pitch motion of the vessel is important and that the remaining degrees of freedom can be neglected.

The model assumes that ramming interaction consists of two main parts, namely crushing of the ice edge during penetration, followed by the ship bow sliding up

onto the ice floe. The normal component of the ramming force can be determined using equation (3.4).

$$F_n = C_s v_{ship} \sin^{0.2} \varphi_s \sqrt{\Delta A_{wp}} \tag{3.4}$$

The parameter C_s depends on the compressive strength of the ice, while the other parameters are related to the vessel geometry and velocity.

Ice ramming forces acting on the vessel USCG Polar Sea have been analysed by [Chen et al., 1990] using measurement data from sea trials. An analytical force-time model was compared with measured data using finite element analyses, and the agreement was good. Measurement data suggested that the duration of each force peak would not exceed 1.0-1.5 s.

There exist several models for impact between vessels and smaller ice features that are not assumed massive compared to the vessel. However, such models are not valid for ramming of ice ridges and are therefore not considered further.

Chapter 4

Review of Ice Classes

When it comes to classification of ships going in ice-infested waters, there exist design rules put forth by each major classification society. Some of these societies include *American Bureau of Shipping*, *Det Norske Veritas* and *Germanischer Lloyd*. In general, the classification society rules are more or less equivalent and based on the original *Finnish–Swedish Ice Class Rules* applied in the Baltic waters [Riska, 2011]. However, when designing ships for Arctic conditions, Baltic design rules come short in terms of strength and performance requirements because of the increased ice actions experienced in Arctic regions. The *International Association of Classification Societies* therefore established a separate set of design rules for ships going in Arctic waters. DNV has also developed design rules for vessels operating in the Arctic region.

In the following chapter, a brief review of the different ice class notations for ships is given with emphasis on the *DNV Rules for Classification of Ships* and the *IACS Unified Requirements for Polar Ships*. Also, a comparison of the design load scenarios adapted in DNV Arctic classes and IACS Polar classes is made.

4.1 DNV Ice Classes

Det Norske Veritas has included their design rules for ships going in ice-infested waters as a part of their general ship rules [DNV, 2011]. The class notations are categorized into groups according to the severity of the ice conditions in the area of intended vessel operation. The two lowest DNV ice classes *ICE-C* and *ICE-E* are intended for basic ice strengthening and are applicable for vessels operating in waters with light ice conditions.

DNV also has some special notations related to cold climate that can be assigned to vessels separate from the main ice class. The *Sealer* notation is applicable for vessels specially designed for catching in cold regions where navigation in pack

ice is required. Further, the *WINTERIZED* notation is suited for winterization of vessels intended for operation in cold climate environments where icing is an important concern. Finally, the *DAT(-X° C)* notation is applicable for materials in vessels intended to operate for longer periods in areas where the air temperature is low.

4.1.1 Ice Classes for the Baltic Region

Vessels that are designed to operate in the Baltic region will be exposed to ice actions that demand better strengthening than what is required to obtain the two lowest DNV ice classes. Like many other classification societies, DNV has adapted the Finnish–Swedish Ice Class Rules as a basis for their Baltic ice class notations.

DNV Class	Corresponding Finnish–Swedish Ice Class	Ice thickness limit
ICE-1A*	IA Super	1.0 m
ICE-1A	IA	0.8 m
ICE-1B	IB	0.6 m
ICE-1C	IC	0.4 m

Table 4.1: DNV Baltic ice classes

Table 4.1 shows the DNV ice classes for the Baltic region and corresponding Finnish–Swedish ice classes along with the maximum level ice thickness during operation. In practice, the difference between the two highest classes *ICE-1A* and *ICE-1A** is that vessels with the latter class notation normally do not require ice breaking assistance.

4.1.2 Ice Classes for the Arctic Region

The strictest ice class notations in terms of strength and performance requirements are those applicable for vessels going in Arctic waters. The DNV Arctic ice classes are comparable to the Polar ice classes developed by IACS, and will therefore be discussed in more detail.

Table 4.2 gives an overview of the Arctic ice classes and a description of the types of ice features that are to be encountered during operation. The *ICE-xx* class notations are applicable when no ramming of pressure ridges is anticipated, while vessels with the *POLAR-xx* class notations can tolerate occasional ramming. Minimum ramming speeds for the *POLAR* ice classes are given in table 4.3. It is also worth mentioning that the number *-xx* in the Arctic class notations is directly linked to the average ice thickness to be encountered, as seen in table 4.2.

If a vessel is designed for ice breaking operation, the additional class notation *Icebreaker* can be assigned together with the *ICE* or *POLAR* notations. The *Icebreaker* notation is applied when repeated ramming is expected.

Class notation	Average ice thickness	Average ice strength	Ice features encountered
POLAR-30	3.0 m	10.0 MPa	Pressure ridges, multi-year ice floes and glacial ice inclusions
POLAR-20	2.0 m	8.5 MPa	
POLAR-10	1.0 m	7.0 MPa	
ICE-15	1.5 m	7.0 MPa	Winter ice with pressure ridges, no ramming
ICE-10	1.0 m	5.6 MPa	
ICE-05	0.5 m	4.2 MPa	

Table 4.2: DNV Arctic ice classes

Ice class	Minimum ramming speed
POLAR-30	4.0 m/s (7.8 knots)
POLAR-20	3.0 m/s (5.8 knots)
POLAR-10	2.0 m/s (3.9 knots)

Table 4.3: Minimum ramming speed for *POLAR* classes

4.1.3 Design Loads for Arctic Ice Classes

In the following, an overview of the design loads adapted for DNV Arctic classes is given with focus on the relevant scenarios for coastguard vessel KV Svalbard, which has the notation *Icebreaker POLAR-10*. Other structural requirements such as local and global strength criteria for plates, stiffeners and frames are also of importance, but will not be considered further. Different parameters will be defined continuously as they first appear in the design equations since many parameters reappear throughout the design rules.

There are several important design load scenarios for vessels going in ice-infested waters, including bow impact forces, beaching forces, ice compression loads, local ice pressure and ice-induced accelerations. However, only design rules related to bow ramming impact forces and local ice pressure on the hull will be described.

The vertical component of the design force due to a head-on ramming impact is given by equation (4.1):

$$P_{ZR} = P_R F_{EL} \quad [\text{kN}] \tag{4.1}$$

where P_R and F_{EL} are given by equations (4.2) and (4.3), respectively:

$$P_R = 28 \left(\frac{C_R E_{imp}}{\tan \gamma} \right)^{0.6} (\sigma_{ice} \tan \alpha)^{0.4} \tag{4.2}$$

$$F_{EL} = \sqrt{\frac{E_{imp}}{E_{imp} + C_L P_R^2}} \tag{4.3}$$

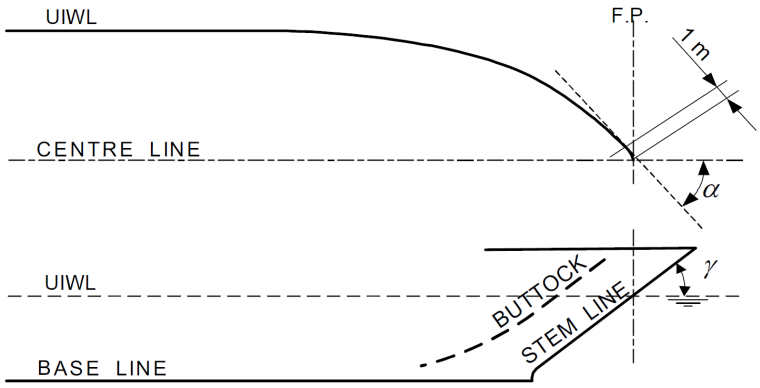

Figure 4.1: Bow angle definitions [DNV, 2011]

Bow angles α and γ from the equations above are explained in figure 4.1 and the ice strength σ_{ice} is given in table 4.2 for the relevant ice class. The coefficient C_R is taken equal to 2 for vessels with the *Icebreaker* notation. Also, the impact energy E_{imp} is expressed as a function of the vessel's kinetic energy prior to ramming E_{ke}:

$$E_{imp} = E_{ke} \frac{\tan^2 \gamma}{\tan^2 \gamma + 2.5} \quad \text{[kNm]} \tag{4.4}$$

Further, the coefficient C_L is given by:

$$C_L = \frac{L^3}{3 * 10^{10} I_V} \tag{4.5}$$

where L is the ship length (m) and I_V is the moment of inertia (m^4) about the horizontal neutral axis of the midship section.

For vessels with spoon-shaped bows such as KV Svalbard, the following relation between bow angles α and γ is valid:

$$\tan \alpha = 1.2 \frac{B^{0.1}}{\sqrt{\cos \gamma}} \tag{4.6}$$

where B is the vessel breadth (m).

As previously stated, local ice pressure on the hull plating is important in Arctic design, and the rules present a pressure requirement of:

$$p = p_0 F_B \quad \text{[kPa]} \tag{4.7}$$

where p_0 is defined as the basic ice pressure:

$$p_0 = 1000 F_A \sigma_{ice} \quad [\text{kPa}] \tag{4.8}$$

The parameter F_A is a correction factor depending on which location on the hull is in question, and is generally taken equal to unity when considering the bow and stem area and 0.6 when considering the midship area. For vessels with the *Icebreaker* notation, F_A is taken equal to 0.2 when considering the bottom area and 0.8 when considering the stern area.

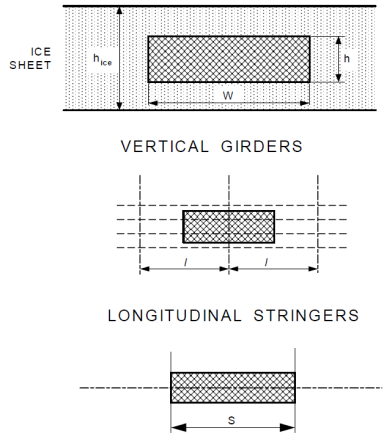

Figure 4.2: Definition of design contact areas [DNV, 2011]

The factor F_B corrects for the size of the design contact area A_C and can be expressed as:

$$\begin{aligned} F_B &= \frac{0.58}{(A_C)^{0.5}} \qquad \text{for } A_C \leq 1.0 \text{ m}^2 \\ F_B &= \frac{0.58}{(A_C)^{0.15}} \qquad \text{for } A_C > 1.0 \text{ m}^2 \end{aligned} \tag{4.9}$$

The size of the design contact area varies according to the frame arrangement in the part of the hull in question, and can therefore be a function of the spacing between frames, girders, stringers or stiffeners. In general, the area is taken as a rectangular patch $A_C = h * w$ (m^2), as displayed in figure 4.2.

4.2 IACS Polar Classes

The IACS Polar classes are based on a separate set of design rules compared to the DNV ice classes, and there is no distinction between the geographical area in which the vessel is to operate. IACS has established seven polar classes, each

with increasing requirements with respect to operational capability and strength [IACS, 2011]. Table 4.4 provides a description of the anticipated ice conditions for each polar class based on the nomenclature from [WMO, 1970].

Polar Class	Ice description
PC-1	Year-round operation in all Polar waters
PC-2	Year-round operation in moderate multi-year ice conditions
PC-3	Year-round operation in second-year ice which may include multi-year ice inclusions
PC-4	Year-round operation in thick first-year ice which may include old ice inclusions
PC-5	Year-round operation in medium first-year ice which may include old ice inclusions
PC-6	Summer/autumn operation in medium first-year ice which may include old ice inclusions
PC-7	Summer/autumn operation in thin first-year ice which may include old ice inclusions

Table 4.4: IACS Polar ice classes

Vessels in compliance with the requirements of Polar class *PC-6* or *PC-7* may be granted DNV class notation *ICE-1A** or *ICE-1A*, respectively, provided that the engine output is sufficiently high.

4.2.1 Design Loads for Polar Classes

For vessels with Polar class notation given by IACS, the governing load scenario for determining necessary scantlings is a glancing impact on the bow. The design load is characterized by the average ice pressure and the corresponding load patch area. Further, it is distinguished between impact on the bow area and possible impacts in areas other than the bow. Only bow impact will be further addressed.

To determine the average pressure and the load patch area, it is necessary to calculate a set of ice load parameters, namely the *shape coefficient* fa, *total glancing impact force* F, *line load* Q and *pressure* P. For the bow region, a load patch aspect ratio AR is also determined from equation (4.10) based on the hull angles given in figure 4.3.

$$AR_i = 7.46 \sin \beta_i' \geq 1.3 \tag{4.10}$$

For the bow area, the shape coefficient is determined according to equation (4.11):

$$fa_i = \min(fa_{i,1}; fa_{i,2}; fa_{i,3}) \tag{4.11}$$

where:

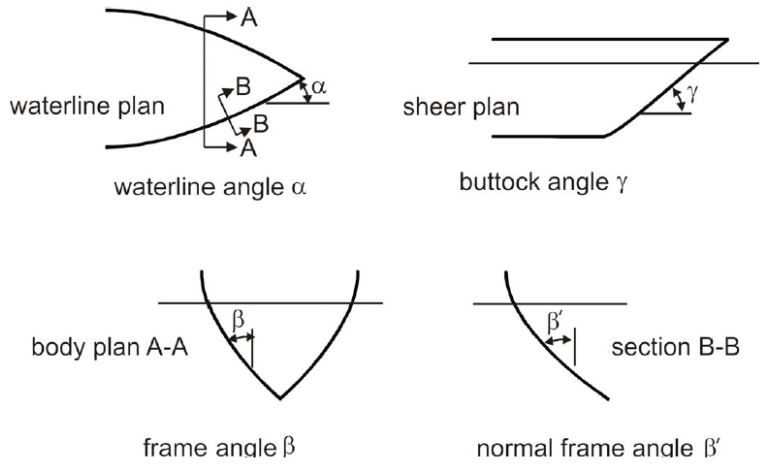

Figure 4.3: Definition of hull angles [IACS, 2011]

$$
\begin{aligned}
fa_{i,1} &= \left(0.097 - 0.68\left(\tfrac{x}{L_{wl}} - 0.15\right)^2\right)\tfrac{\alpha_i}{\sqrt{\beta_i'}} \\
fa_{i,2} &= \tfrac{1.2CF_F}{CF_C(\Delta_{tk})^{0.64}\sin\beta_i'} \\
fa_{i,3} &= 0.60
\end{aligned}
\tag{4.12}
$$

In the equations above, x is the distance (m) from the forward perpendicular to the region in question, L_{wl} is the ship length (m) measured at the upper ice waterline and i is the sub-region of the bow under consideration. When determining the ice load parameters, the bow is divided into four sub-regions of equal length along the waterline.

Further, CF_F and CF_C are the *Flexural* and *Crushing Failure Class Factors*, respectively. These factors are tabulated in the design rules and depend on the desired polar class. Finally, Δ_{tk} is the ship displacement (kt) at the UIWL, which should not be taken less than 5 kt.

The total glancing impact force for the bow area is determined by equation (4.13):

$$F_i = fa_i CF_C\left(\Delta_{tk}\right)^{0.64} \quad \text{[MN]} \tag{4.13}$$

Further, the line load for the bow area is estimated from equation (4.14):

$$Q_i = \frac{F_i^{0.61} CF_D}{AR_i^{0.35}} \quad \text{[MN/m]} \tag{4.14}$$

where the parameter CF_D is the *Load Patch Dimensions Class Factor*, as tabulated in the design rules.

Finally, the bow area pressure is determined according to equation (4.15):

$$P_i = F_i^{0.22} CF_D^2 AR_i^{0.3} \quad \text{[MPa]} \tag{4.15}$$

When the ice load parameters from the equations above are determined for each sub-region i of the bow area, the maximum values of the four sub-regions are taken to represent the whole bow area by the parameters F_{Bow}, Q_{Bow} and P_{Bow}. From these three parameters, the design load patch of the bow region is determined as a rectangular area with height and width according to equation (4.16):

$$\begin{aligned} b_{Bow} &= Q_{Bow}/P_{Bow} \quad \text{[m]} \\ w_{Bow} &= F_{Bow}/Q_{Bow} \quad \text{[m]} \end{aligned} \tag{4.16}$$

Once the load patch dimensions b_{Bow} and w_{Bow} are determined, the average pressure within the design load patch is calculated using equation (4.17):

$$P_{avg} = \frac{F_{Bow}}{b_{Bow} * w_{Bow}} \quad \text{[MPa]} \tag{4.17}$$

It is important to mention that the pressure calculated according to equation (4.17) is the *average* pressure over the design load patch. Areas of higher concentrated pressure will exist within the load patch, and the local pressure will generally increase as the area decreases. This effect is accounted for using *peak pressure factors* that are tabulated in the design rules.

4.3 Comparative Study

As seen from the discussion on class notations, DNV divides different ice classes into groups according to geographical region. The classes are further subdivided based on the nominal level ice thickness and the limiting impact conditions. The IACS Polar classes are intended for vessels navigating in ice-infested waters independent of geographical region. The classes are separated with respect to varying operational capability and strength requirements based on the expected ice conditions.

One can observe several differences between the structural requirements of the DNV Arctic classes and the IACS Polar classes. Firstly, while DNV defines several different design load scenarios, IACS operates with the glancing impact load on the bow only. Secondly, DNV calculates the contact area between ice and vessel based on hull dimensions, independent of design ice loads. IACS, on the other hand,

determines ice pressure and load patch dimensions based on a defined set of ice load parameters that characterize the glancing impact load. This suggests that the DNV design rules are more specific when it comes to governing design scenarios, while the IACS design rules are more general in terms of vessel type and prevailing ice conditions.

Chapter 5

Dynamic Response Analyses

In order to assess the dynamic response of a vessel due to ice ridge ramming, two separate finite element models have been established. The models are intended to represent the coastguard vessel KV Svalbard, which has been employed in the ILM project by DNV. Throughout the project lifetime, several sea trials have been conducted where response measurements in ice-infested waters have been recorded. In the following, the scope of the analyses will be presented along with a description of the models and tools that are applied.

5.1 Scope of Analyses

The models that have been established include a simplified two-dimensional beam model of the hull girder and a more detailed three-dimensional shell model of the hull structure. The intention is to analyse dynamic response using both models, and to investigate possible discrepancies in the results. Dynamic, as well as quasi-static response analyses will be performed in order to study the possibility of dynamic amplification. Comparisons will be made with respect to the heave displacement in the bow region after impact between vessel and ice ridge.

Further, parameter variations with respect to inertia and damping models, as well as solution methods, will be carried out in order to study the influence of these parameters on the results. Different pulse shapes are also studied in relation to the load modelling. The parametric study will only be carried out by use of the simplified FE model.

In order to verify the validity of the models, full scale measurements from a ramming sequence with KV Svalbard will be analysed and compared with the model results.

5.2 Software

In the following, a brief description of the software used for analyses will be given.

5.2.1 Patran-Pre

Patran-Pre is a pre-processor for FE applications. The large number of available modelling and meshing tools included in the pre-processor makes it well-suited for establishing models with complicated geometry, such as a ship hull. After creating a model with Patran-Pre, the program will generate an input-file for the desired FE-solver, in this case *Abaqus Standard*.

5.2.2 Abaqus CAE

The software package *Abaqus CAE* is a complete FE program, including pre-processor, FE-solvers and post-processor. The Abaqus pre-processor is somewhat limited compared to Patran-Pre, and is therefore mostly used for creating simple models and geometries. However, the various Abaqus FE-solvers support a wide variety of element formulations and can perform many different types of FE analyses, including non-linear problems.

The Abaqus software is based on the programming language *Python*, meaning that an analysis consists of a set of specific Python commands that are executed in order. By creating a Python-script containing the commands necessary for a specific analysis, it is possible to run a large number of serial analyses in batch mode, thus requiring no manual input from the user. This is very advantageous when performing parametric studies, where an analysis has to be repeated several times while varying the value of one or more parameters. It is also preferred when the analysis includes a large number of load cases. Python-scripts have been developed for the various KV Svalbard FE models.

5.2.3 MATLAB

The software package *MATLAB* is a large mathematical toolbox widely used for processing data. Using the many built-in functions in MATLAB, it is possible to post-process results from FE analyses in an efficient way.

MATLAB can also run system commands such as executing a Python-script in Abaqus. This makes it possible to automate the process of running several Abaqus analyses, followed by post-processing of the output data directly in MATLAB. A set of MATLAB-scripts and -routines have been developed in order to increase the efficiency when running analyses with the KV Svalbard FE models.

5.3 KV Svalbard

KV Svalbard is a Norwegian coastguard vessel with the DNV class notation Icebreaker POLAR-10. Main particulars necessary for establishing FE models are given in table 5.1, with reference to the general arrangement drawing of the vessel.

Overall length	103.7 m
Waterline length	94.54 m
Breadth moulded	19.1 m
Waterline breadth	18.56 m
Draught	6.5 m
Displacement	6530 t

Table 5.1: Main particulars of KV Svalbard

Important parameters that are not given will either be calculated using appropriate methods or determined based on qualified assumptions.

In order to perform accurate dynamic analyses, it is necessary to calculate some important quantities such as the hydrodynamic added mass and hydrostatic stiffness of the vessel. Also, the section modulus of the hull girder must be determined in order to obtain a satisfying stiffness representation for the simplified beam model.

5.3.1 Hydrodynamic Added Mass

The hydrodynamic added mass of a vessel is a result of the vessel oscillating in water. It gives rise to an external force that is proportional to the acceleration of the vessel, and the effect is equivalent to a substantial increase of the vessel's mass. The force resulting from added mass is defined as follows [Faltinsen, 1990]:

$$F_i = -A_{ij}\frac{d^2\eta_j}{dt^2} \tag{5.1}$$

Equation (5.1) expresses the force in direction i due to acceleration in direction j, and the quantity A_{ij} is defined as the hydrodynamic added mass coefficient.

Added mass is in general a function of the oscillating frequency of the vessel in water. However, due to the short duration of ramming force pulses, it is assumed that the added mass can be determined based on the limit value when the oscillating frequency approaches infinity. Further, it is assumed that the added mass in the vertical direction, which is proportional to heave acceleration, is dominant.

The two-dimensional added mass coefficient of the vessel mid-ship section is determined based on figure 5.1. Using a geometry model of KV Svalbard provided by DNV, the ratio of mid-ship sectional area to the product of the breadth and draught is determined to be approximately 0.90. This yields the following result:

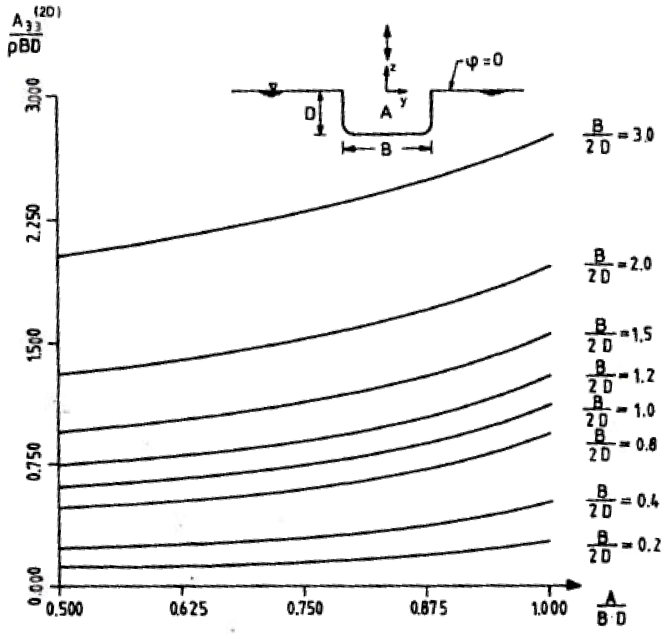

Figure 5.1: Two-dimensional heave added mass for infinite oscillation frequency based on Lewis form [Faltinsen, 1990]

$$\frac{A_{33}^{2D}}{\rho BD} = 1.10 \tag{5.2}$$

The parameter A_{33}^{2D} presented in equation (5.2) is the two-dimensional added mass coefficient of the mid-ship section. In order to apply *strip theory*, one has to determine the corresponding coefficient for all sections of the vessel and perform an integration along the ship length [Faltinsen, 1990]. This can be very time-consuming, and if A_{33}^{2D} is assumed constant for all ship sections, the error introduced will be rather significant. It is therefore assumed that the result of equation (5.2) can approximate the ratio of added mass to actual mass per unit length of each section, and that this ratio is constant for all ship sections.

From the discussion above, it is implicitly assumed that the total mass of the vessel, including hydrodynamic added mass, is given by:

$$M_{total} = (1 + 1.10)\,\Delta = 13713 \quad [\text{t}] \tag{5.3}$$

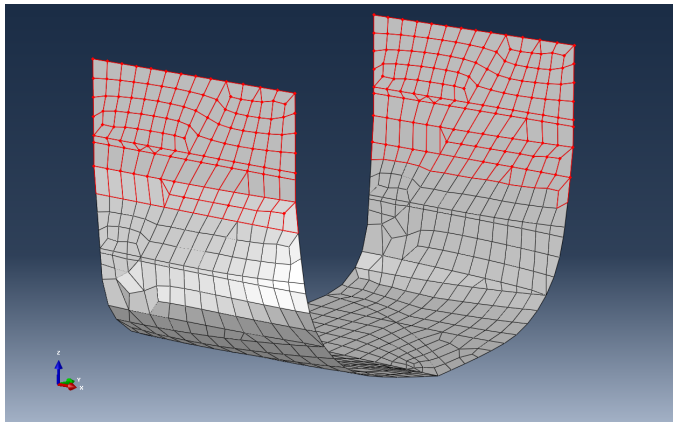

Figure 5.2: KV Svalbard mid-ship section, waterline approximately highlighted

5.3.2 Hydrostatic Stiffness

The hydrostatic stiffness of a vessel is a result of its buoyancy in water, which gives rise to an external force proportional to the vertical displacement from equilibrium position. The hydrostatic restoring force is defined as [Faltinsen, 1990]:

$$F_i = -C_{ij}\eta_j \tag{5.4}$$

A free-floating vessel will only have hydrostatic restoring forces in three degrees of freedom, namely heave, pitch and roll. When ice ramming forces acting head-on are considered, only heave and pitch motion will be present due to centerline symmetry. In the present analysis, it is for simplicity assumed that hydrostatic stiffness in the heave direction is dominant, and that pitch stiffness can be neglected.

In order to determine the hydrostatic stiffness, it is necessary to estimate the waterplane area of the vessel. This is done with Abaqus using the aforementioned geometry model of the KV Svalbard hull.

Due to difficulties in determining the area at the exact waterline, the area is determined for the deck at 5400 ABL and scaled using the length and breadth of the vessel, resulting in a waterplane area of 1466 m^2. Detailed calculations are described in appendix A. The hydrostatic stiffness can then be determined using the following equation [Faltinsen, 1990]:

$$C_{33} = \rho g A_{wp} = 14.74 \quad [\text{MN/m}] \tag{5.5}$$

Once the hydrostatic stiffness and the total mass is known, the natural heave oscillation period can be determined as follows:

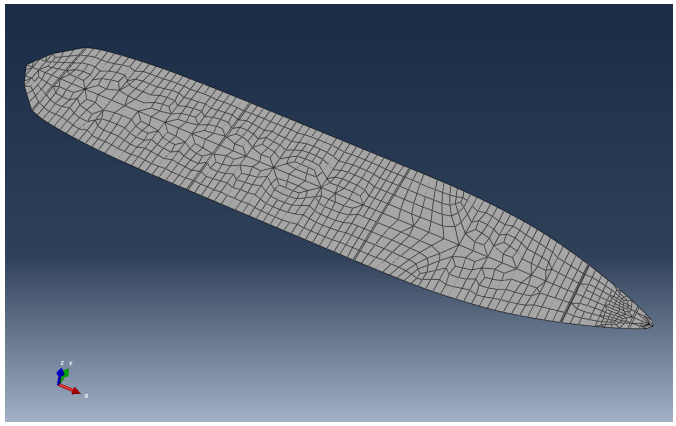

Figure 5.3: KV Svalbard deck at 5400 ABL

$$T_3 = 2\pi\sqrt{\frac{M_{total}}{C_{33}}} = 6.06 \quad [\text{s}] \tag{5.6}$$

5.4 Simplified Model of KV Svalbard

The simplified FE model has been created using the integrated pre-processor in Abaqus CAE. It contains 64 linear two-node Timoshenko beam elements along the overall length of the ship hull. Timoshenko beam elements are formulated using classical beam theory, but with the inclusion of transverse shear deformation [Dassault Systemes, 2011].

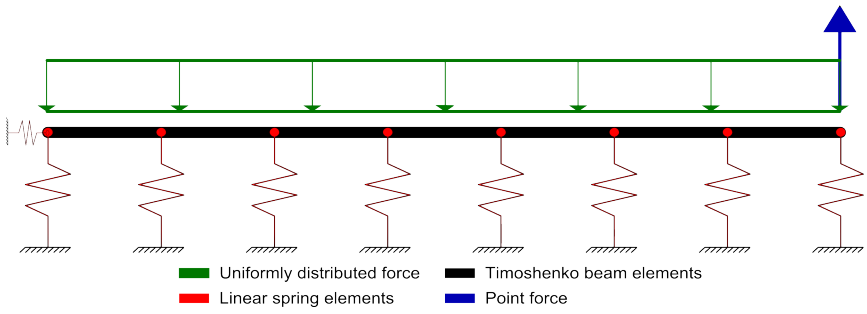

Figure 5.4: Simplified beam model of hull girder with ice ramming force

5.4.1 Cross-Sectional Area

In order to obtain reasonable global bending stiffness for the beam model, the element cross-sectional area has to be determined such that the section modulus and moment of inertia of the hull girder are correct. This is done by assuming a rectangular compact cross-section, and adjusting the height and width to obtain satisfying values.

Since the section modulus and moment of inertia for the vessel are unknown, numerical values for these parameters are determined based on the global strength requirements proposed in [DNV, 2011]. Using classical beam theory, the result is a required cross-sectional height of 5.09 m and a corresponding width of 0.35 m, thus giving a cross-sectional area of 1.8 m^2.

5.4.2 Inertia and Hydrostatic Stiffness

For simplicity, inertia and hydrostatic stiffness are uniformly distributed along the hull girder, as illustrated in figure 5.4. Modelling of inertia properties, including hydrodynamic added mass, has been done by use of an equivalent material density determined based on the cross-sectional area of the beam elements. The required material density to obtain the correct total mass is 73527 kg/m^3. An alternative model where the mass is uniformly lumped at each node has also been established in order to study the importance of mass distribution.

The hydrostatic stiffness of the vessel is modelled using a linear spring element at each beam node, connected to a fixed node at the opposite end of the spring. The axial stiffness is taken equal for each spring element to obtain a uniform buoyancy distribution.

5.4.3 Load Modelling

The ice ramming load is modelled as a time-varying point force acting at the bow node. Since the ramming force mainly acts in the vertical direction, only this component is included in the model, as illustrated in figure 5.4. The maximum force is determined according to [DNV, 2011], giving a magnitude of 24.49 MN, while the time variation of the force magnitude is modelled as a symmetric triangular pulse equivalent to case *a* in figure 3.5. However, several other force-time histories have also been modelled to investigate the effect on dynamic response, as illustrated in figure 6.16.

In order to determine the effect of dynamics during ridge ramming, duration of the force pulse has been systematically varied from 0.25 s to 2.0 s based on recorded data for the vessel USCG Polar Sea [Chen et al., 1990]. The impulse is kept constant for all durations in order to obtain a proper comparison, meaning the force amplitude is decreased with increasing duration.

5.5 Detailed Model of KV Svalbard

As previously mentioned, a geometry model of the KV Svalbard hull has been provided by the ship structures-department at DNV. The model only includes the outer hull plating of the vessel, and extends from baseline to 14800 ABL in the vertical direction. Longitudinally, the model extends along the full length of the hull, but only half of the model is included in the transverse direction due to centerline symmetry.

The geometry model has the file format *IGES* (.igs) and can therefore be imported to Patran-Pre for further modelling and generation of element mesh. Definition of external loads and boundary conditions has been done in Abaqus CAE.

5.5.1 Refinement of Geometry Model

In order to obtain proper global stiffness properties, the four main structural decks of the vessel including tank top have been modelled. The tank top is located at 2750 ABL, while the next three decks are positioned at 5400 ABL, 8300 ABL and 10800 ABL, respectively. To simplify the modelling process, each individual deck is given uniform thickness although this varies somewhat along the vessel length.

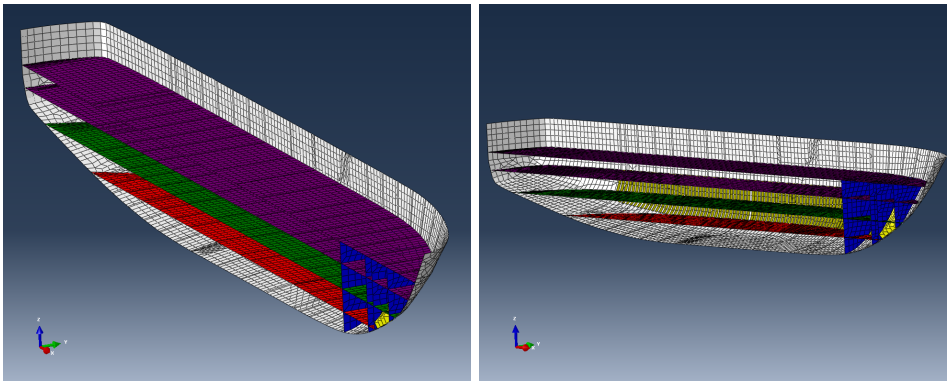

Figure 5.5: Shell model with colour coding according to shell thickness

In addition to main decks, four transverse bulkheads in the bow region have been modelled at ship sections 4, 9, 11 and 19, extending from baseline to 10800 ABL in the vertical direction. The bulkheads have also been assigned uniform thickness corresponding to the average value along the height.

To further improve the global stiffness, transverse frames have been modelled at every ship section except in the stern part, corresponding to the frame spacing of 800 mm. To reduce the complexity of the model, all frames astern of bulkhead 9 have a transverse extension of 450 mm, and a vertical extension from 2750 ABL to 8300 ABL. The frames ahead of bulkhead 9 are modelled perpendicular to the

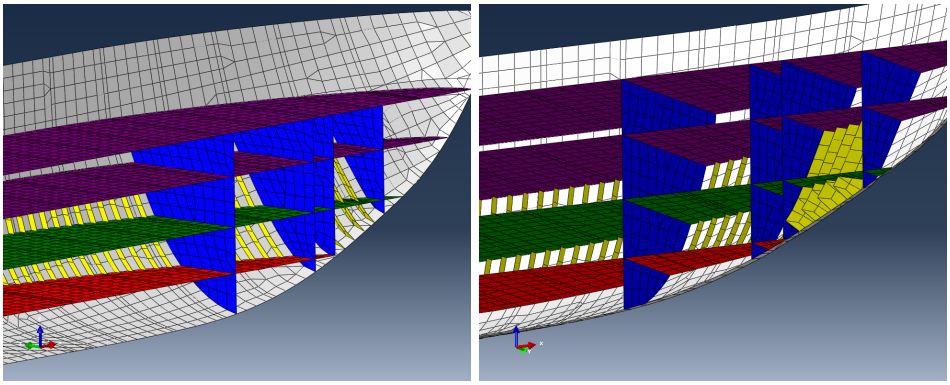

Figure 5.6: Bulkheads and frames with colour coding according to shell thickness

outer hull plating, corresponding roughly to the waterline entrance angle of 63°, which is defined as α in figure 4.1.

Geometric set	Shell thickness	Colour code
Outer plating	40 mm	White
Tank top	9 mm	Red
Deck 5400 ABL	6 mm	Green
Deck 8300 ABL	7 mm	Purple
Deck 10800 ABL	7 mm	Purple
Bulkheads	10 mm	Blue
Frames	15 mm	Yellow

Table 5.2: Thickness assignments in shell model

The thickness assignments of the different geometric sets are given in table 5.2. To get a correct definition of boundary conditions, the half-model is mirrored about the centerline such that the complete hull structure is included in analyses.

5.5.2 Generation of Element Mesh

The refined geometry model has been meshed using Patran-Pre. Quadrilateral four-node shell elements have been applied to the extent allowed by the geometry of the structure, while triangular three-node elements are used only where necessary. This is typically at parts of the hull with large geometric curvature where quadrilateral elements fail to represent the true geometry.

A total of 21007 elements and 20306 nodes are applied in the modelling, which is assumed to be adequate for the analysis purpose. The element mesh includes 20375 quadrilateral *S4R5* elements and 632 triangular *STRI3* elements.

5.5.3 Inertia and Hydrostatic Stiffness

Since the model only includes major structural elements of the hull, the model mass will be substantially lower than the total mass of the vessel. To compensate for this difference, an equivalent material density of 65340 kg/m^3 has been applied in a similar fashion as for the beam model. However, the mass will be distributed in a more correct manner due to the increased degree of detail in the model.

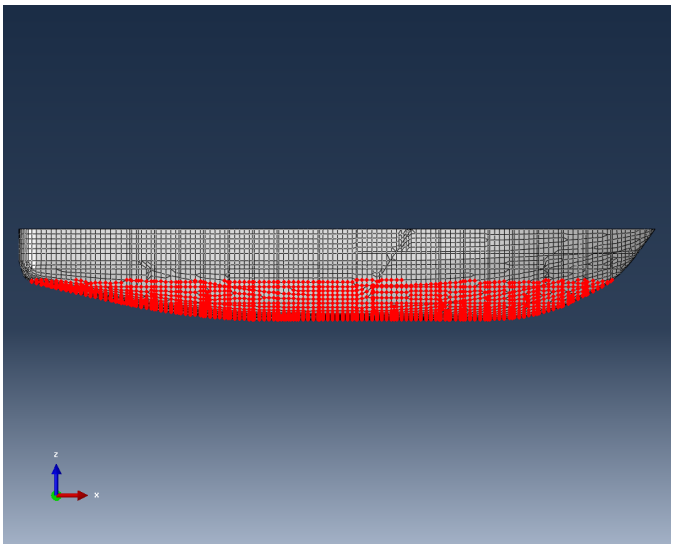

Figure 5.7: Nodes where linear spring elements are connected

Modelling of the hydrostatic stiffness has been done by addition of linear spring elements at all nodes below the waterline. Axial stiffness is taken equal for all springs, but the buoyancy distribution will be more correct as the number of nodes at each ship section depends on the breadth of the hull at that particular position. Figure 5.7 shows the distribution of buoyancy springs on the submerged part of the hull.

5.5.4 Load Modelling

The ice ramming load is modelled as a uniform pressure with time-varying magnitude acting on every element within the load patch displayed in figure 5.8. The area of the load patch is approximately 1.82 m^2, and the exact value is a result of the element shapes in the bow region. In order to apply the same global load as for the beam model, the magnitude of the pressure is taken such that the resultant force is approximately equal in both models.

The symmetric triangular pulse shape has been applied in the same manner as for

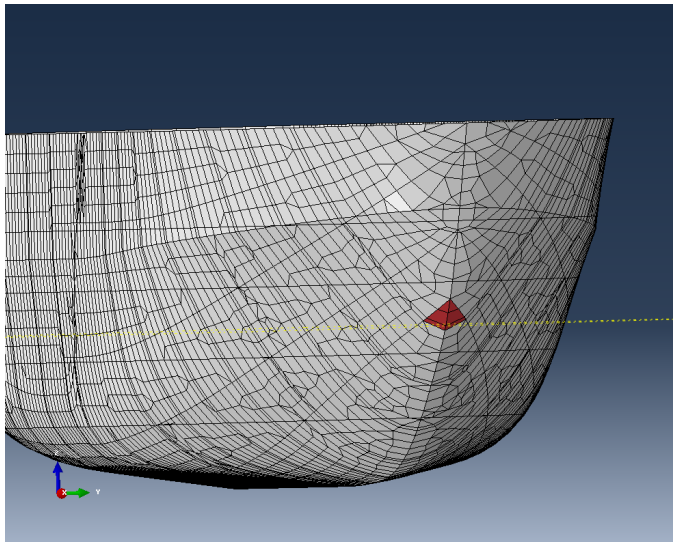

Figure 5.8: Load patch where uniform pressure is applied

the beam model, with pulse duration ranging from 0.25 s to 2.0 s. This makes it possible to compare the results from both models in a proper manner.

Chapter 6

Analysis of Results

To investigate the possibility of dynamic amplification during ice ridge ramming, dynamic and quasi-static response analyses have been carried out for both FE models of the KV Svalbard hull. A parametric study has also been performed to examine the influence of several parameters on the results. In the following, results from the analyses will be discussed and the two models will be compared.

6.1 Identification of Natural Modes

When performing dynamic response analyses, it is important to be aware of the natural modes of vibration, or *eigenmodes*, present in the system, and the frequency intervals at which the modes can become excited. In general, modes with the lowest natural frequencies will have highest energy content, and are therefore most important to consider.

Mode	Natural frequency [rad/s]	Natural period [s]	Comment
1	1.035	6.07	Rigid body heave
2	1.050	5.99	Rigid body pitch
3	5.197	1.21	2-node bending
4	13.845	0.45	3-node bending
5	26.492	0.24	4-node bending
6	47.582	0.15	5-node bending
7	51.046	0.12	Rigid body surge
8	61.602	0.10	6-node bending

Table 6.1: Characteristics of beam model eigenmodes

Figure 6.1 shows the shape of the eight lowest eigenmodes present in the simplified beam FE model. The natural frequencies of the modes are given in table 6.1 and

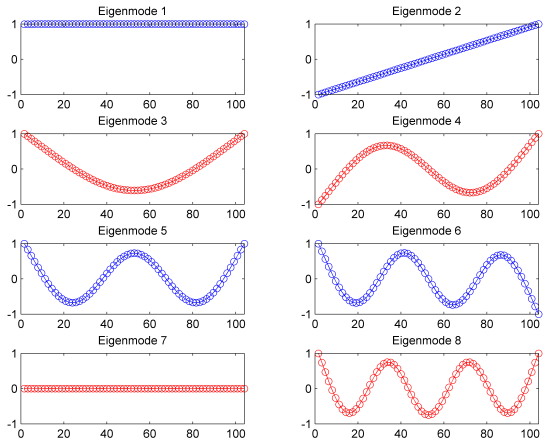

Figure 6.1: Shapes of the lowest beam model eigenmodes

displayed graphically in figure 6.2, and it is observed that the numerical value for the first mode agrees well with the analytical result of equation (5.6).

As can be further observed, mode 7 is the rigid body surge motion, which is not a physical mode of vibration due to lack of longitudinal restoring forces. The reason for the mode appearing in the model is a longitudinal spring element placed at the stern node, which is included to ensure numerical convergence of the analyses. However, it will later be shown that the energy content of mode 7 is negligible, and the presence of the mode is therefore not a problem.

6.1.1 Determination of Damping Parameters

Once the natural modes of the model are identified, damping can be introduced at modal level by applying the concept of *Rayleigh damping* prior to performing response analyses. The basic assumption of Rayleigh damping is that the damping matrix is proportional to the mass and stiffness matrices through the relation:

$$\overline{C} = \alpha\overline{M} + \beta\overline{K} \tag{6.1}$$

The Rayleigh coefficients α and β are determined as follows [Bergan et al., 1983]:

$$\begin{aligned} \alpha &= \frac{2\omega_i\omega_j}{\omega_j^2-\omega_i^2}\left(\zeta_i\omega_j - \zeta_j\omega_i\right) \\ \beta &= \frac{2}{\omega_j^2-\omega_i^2}\left(\zeta_j\omega_j - \zeta_i\omega_i\right) \end{aligned} \tag{6.2}$$

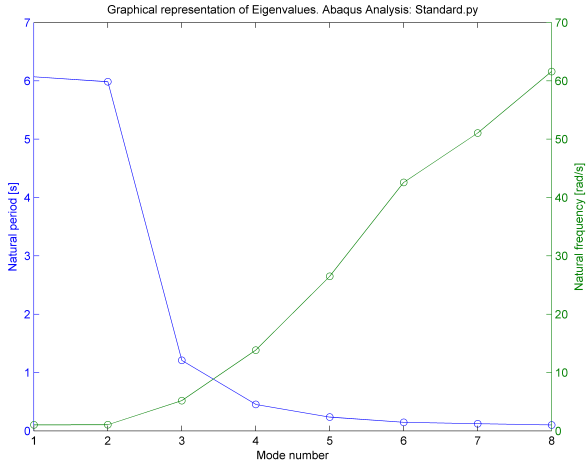

Figure 6.2: Numerical values of beam model eigenmodes

It is in general difficult to determine the damping characteristics of a system. However, due to the transient and pulse-like nature of ice ramming, damping is considered to be of less importance. In the analyses performed by [Chen et al., 1990], Rayleigh damping corresponding to 5 % of *critical damping* was applied for the two-node bending mode. In the present analyses, the same critical damping ratio is therefore assumed for both two- and three-node bending modes, resulting in the modal damping characteristics displayed in figure 6.3.

Since the number of natural modes is proportional to the number of degrees of freedom in a model, it is evident that the detailed shell FE model will contain a vast amount of natural modes compared to the beam model. In order to simplify damping calculations, the same Rayleigh coefficients are applied for both FE models.

6.2 Response Analyses

Dynamic and quasi-static response analyses have been conducted to investigate the possibility of dynamic amplification of the hull structure response during ice ramming. Dynamic response will include effects of inertia and damping, while quasi-static response only considers equilibrium between external loads and internal forces from elastic deformation of the structure. Depending on the relationship between excitation frequency and natural frequency, the inertia of the structure may reduce or amplify the response.

Analyses have been carried out using both FE models by applying a symmetric triangular load pulse. The pulse duration has been varied in the range 0.25-2.0 s

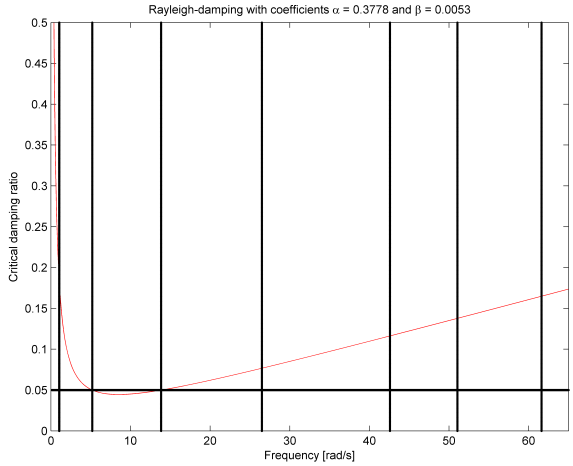

Figure 6.3: Rayleigh damping characteristics applied in dynamic analyses (vertical lines correspond to the natural frequencies)

while keeping the impulse constant such that the peak force corresponds to the design ramming force of 24.49 MN when the pulse duration is equal to 1 s.

6.2.1 Dynamic Response

All dynamic analyses have a duration of 5 s so that possible delayed response following the ramming load can be captured. The time increment applied in all analyses is set equal to 0.01 s. Modal superposition has been applied as solution technique for the simplified beam model, while implicit time integration has been used for the detailed shell model.

Simplified beam model

Figure 6.4 shows time series of vertical displacement at the bow node obtained from the simple beam model. It can be observed that the response history fluctuates more at lower pulse durations, but becomes smoother as the duration is increased. This is explained by the fact that shorter pulses can excite modes with higher natural frequencies, such as the two-node bending mode, while longer pulses will mainly excite the rigid body heave and pitch modes.

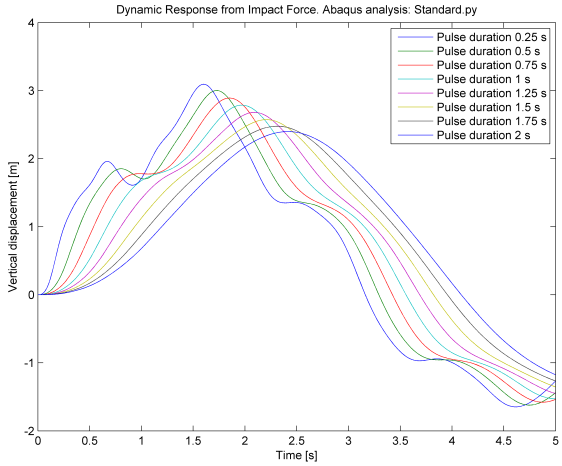

Figure 6.4: Time series of dynamic response from simple beam model

By applying a *fast Fourier transform* algorithm developed for usage in MATLAB [Brodtkorb et al., 2000], time series are transformed into frequency domain, and the energy content of each frequency component is obtained for the different response histories. Figure 6.5 gives a spectral representation of the dynamic response obtained from the simplified beam model. It is seen that most of the energy is concentrated around the rigid body heave and pitch natural frequencies for the longer force pulses, while the energy content of the two-node bending frequency increases for shorter pulses.

It is observed from figure 6.5 that the energy content is negligible for frequencies larger than approximately 8 rad/s, indicating that it is mainly the rigid body heave and pitch modes and the two-node bending mode that will become excited.

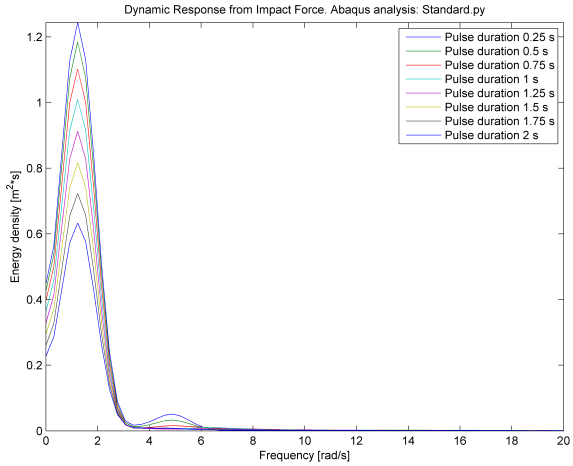

Figure 6.5: Energy spectrum of beam model response in frequency domain

Detailed shell model

Time series of vertical displacement in the bow region of the shell model are displayed in figure 6.6. The response seems to be more or less smooth for both short and long pressure pulses, with the exception of the response from the 0.25 s load pulse. This indicates that excitation of the two-node bending mode is less pronounced for the shell model response, while the domination of rigid body motion is clearly defined.

The frequency composition of the dynamic response obtained from the detailed shell model is presented in figure 6.7. It can be observed that virtually all energy is concentrated around the rigid body heave and pitch natural frequencies. This agrees well with the smoothness of the time series in figure 6.6, which suggests that primarily rigid body modes are excited.

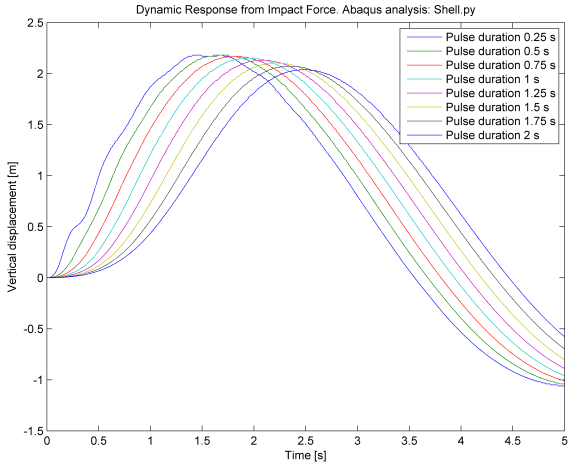

Figure 6.6: Time series of dynamic response from shell model

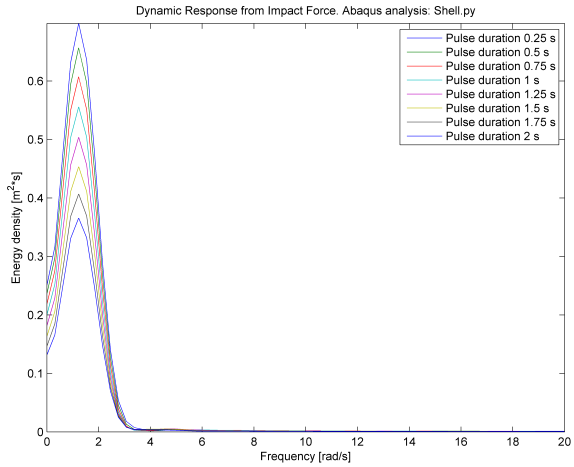

Figure 6.7: Energy spectrum of shell model response in frequency domain

6.2.2 Quasi-Static Response

The quasi-static response analyses have been carried out by preforming a stepwise on-loading of the ice ramming load in a time step corresponding to half of the load pulse duration. The on-loading is followed by a similar stepwise off-loading to represent the symmetric triangular pulse shape applied in the dynamic analyses.

Since inertial and damping effects are not included, the quasi-static response history will also have triangular shape as there is no phase delay between load and response.

Simplified beam model

The quasi-static and dynamic vertical bow displacement for a force pulse with duration 1 s is presented in figure 6.8. As can be seen, the maximum quasi-static response has more than twice the magnitude as that of the maximum dynamic response. Figure 6.8 also shows the time history of the dynamic response scaled by the maximum quasi-static response, and it is seen that the peak dynamic response is approximately 40 % of the quasi-static response for a pulse duration of 1 s.

The ratio of maximum dynamic to maximum quasi-static response, known as the *dynamic load factor*, is shown as a function of force pulse duration in figure 6.9. A linear relationship between the dynamic load factor and the pulse duration can be observed within the investigated duration range, with a coefficient of determination $R^2 = 0.993$. This suggests that the importance of dynamic effects increases with the pulse duration since the duration approaches the natural heave oscillation period, causing an increase in response due to dynamic amplification.

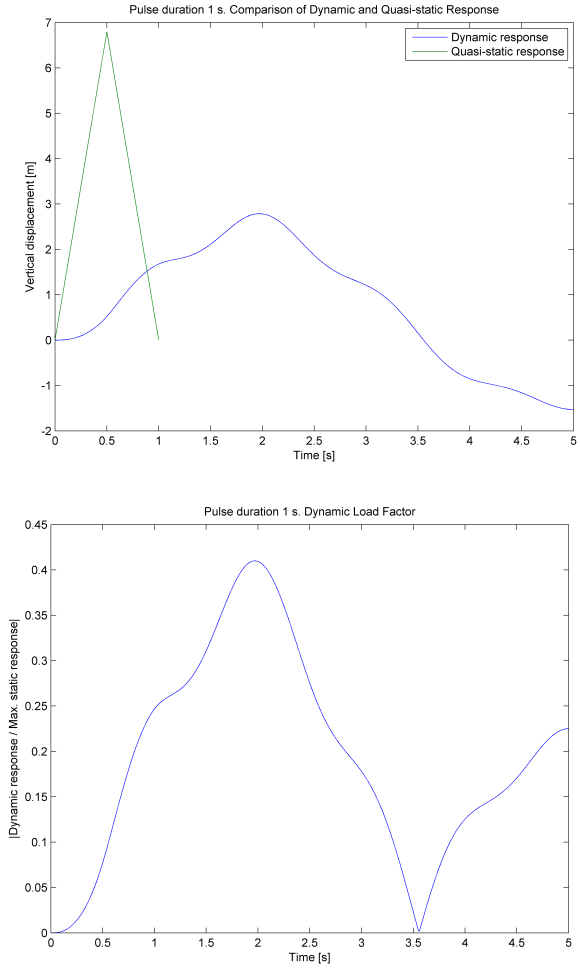

Figure 6.8: Quasi-static and dynamic response from simplified beam model

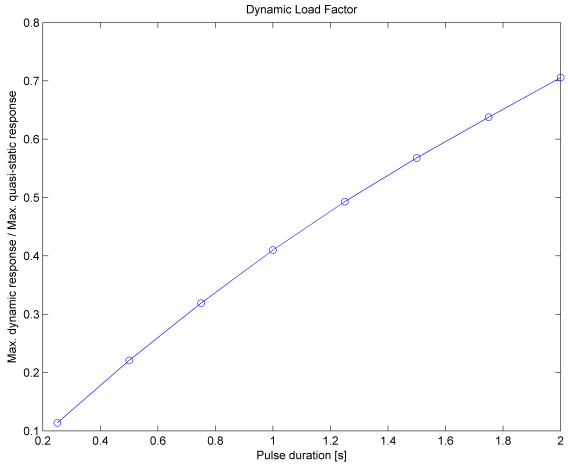

Figure 6.9: Dynamic load factor for simplified beam model

Detailed shell model

Figure 6.10 shows the dynamic and quasi-static vertical bow displacement for a pressure pulse of 1 s obtained from the detailed shell model. It is observed that the maximum dynamic response corresponds to approximately 35 % of the maximum quasi-static response. The dynamic load factor is given in figure 6.11 as a function of pressure pulse duration, and a linear relationship seems to persist in the range 0.25-2.0 s with a coefficient of determination equal to 0.999.

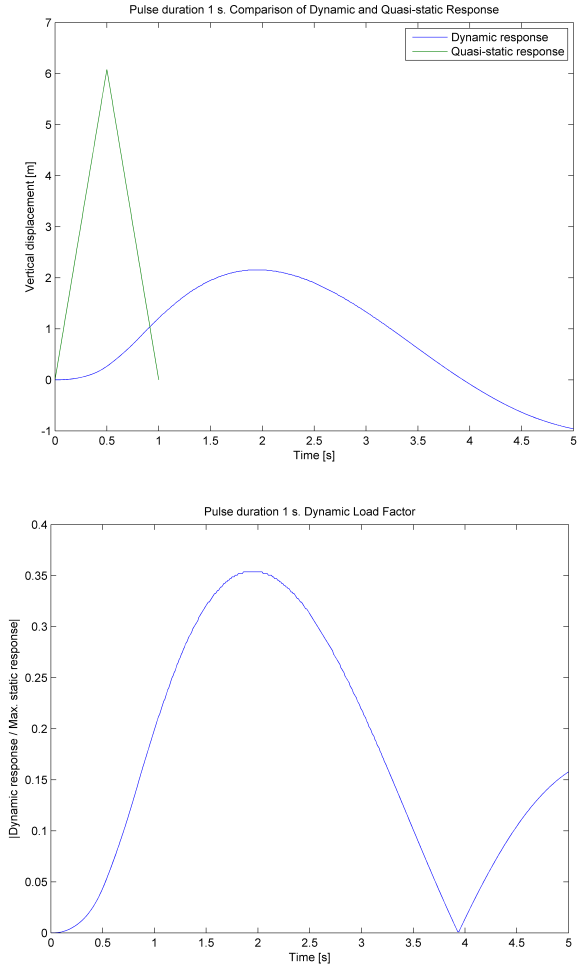

Figure 6.10: Quasi-static and dynamic response from detailed shell model

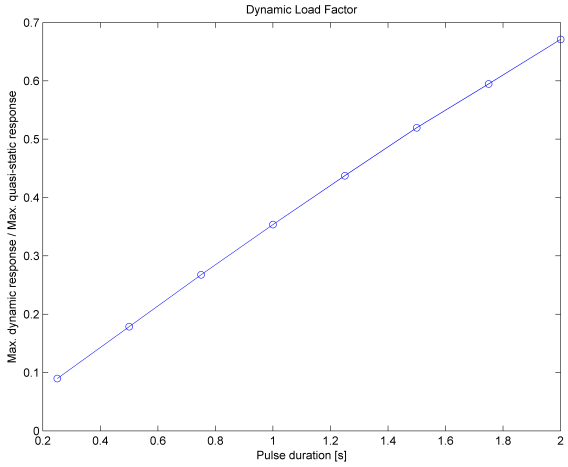

Figure 6.11: Dynamic load factor for detailed shell model

6.2.3 Comparison of Models

Figure 6.12 shows time histories of the vertical bow displacement for a pulse duration of 1 s predicted by the two FE models, and it is seen that the peak response predicted by the beam model is approximately 30 % larger than the peak response from the shell model. Also, the presence of higher order natural modes gives rise to larger fluctuations in the beam model response compared with the smoother shell model response. As previously discussed, this is only an issue for shorter pulse durations. Similar response plots for pulse durations in the range 0.25-2.0 s are given in appendix B.

The most important quantity to observe is perhaps the maximum displacement. Figure 6.13 shows the maximum vertical bow displacement predicted by the two FE models within the investigated pulse duration interval. It is seen that the difference in peak response decreases as the pulse duration increases. For a pulse duration of 0.25 s, the peak vertical bow displacement predicted by the beam model is approximately 40 % larger than the corresponding shell model prediction. In comparison, the peak beam response is only about 18 % larger than the peak shell response for a pulse duration of 2 s.

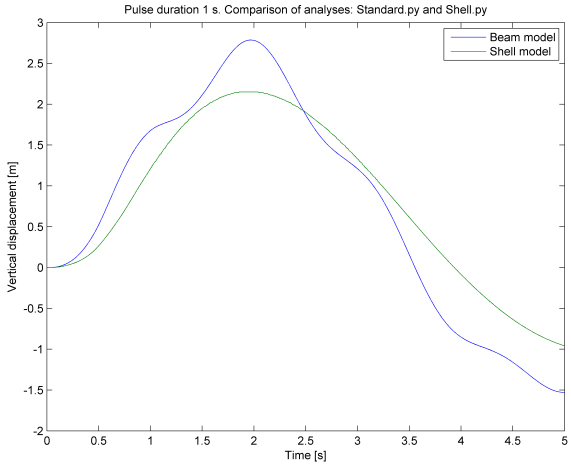

Figure 6.12: Comparison of vertical bow displacement predicted by beam and shell models for 1 s pulse

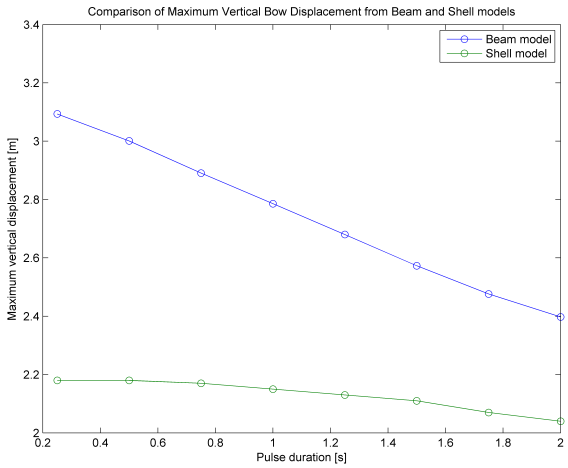

Figure 6.13: Comparison of maximum vertical bow displacement predicted by beam and shell models

The mean displacements of the response histories are also of importance. Figure 6.14 shows the mean vertical bow displacement obtained from the two FE models for the investigated pulse duration interval. It is observed that the difference is smaller than what was observed for the maximum response. For the 0.25 s pulse, the shell model mean response is approximately 16 % larger than that of the beam

model, while for the 2 s pulse, the corresponding value is only 1 %. The result agrees well with the time series shown in figures 6.4 and 6.6, where it is seen that the shell model response on average is larger than the beam model response. This is also clearly seen from the plots given in appendix B.

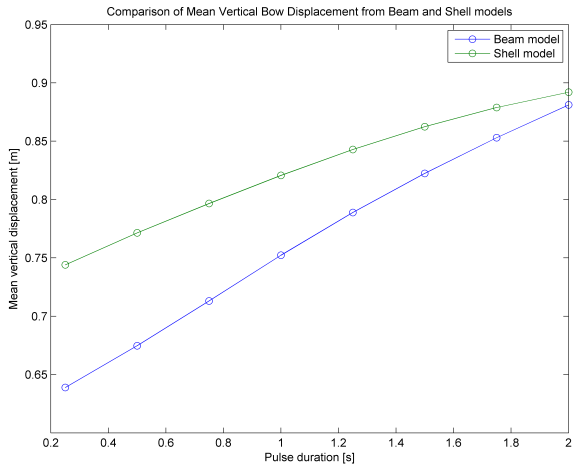

Figure 6.14: Comparison of mean vertical bow displacement predicted by beam and shell models

A comparison of the response variance is given in figure 6.15 for the beam and shell models. It is observed that the difference in variance is fairly constant within the pulse duration interval investigated, where the beam model variance is approximately 82 % larger for the 0.25 s pulse, and 76 % larger for the 2 s pulse. This is in agreement with the differences found in maximum and mean response, where the larger maximum response and lower mean response of the beam model would suggest a larger response variance.

From the previous discussion, a general conclusion is that the beam model predicts larger peak response than that of the shell model. The mean response is however larger for the shell model.

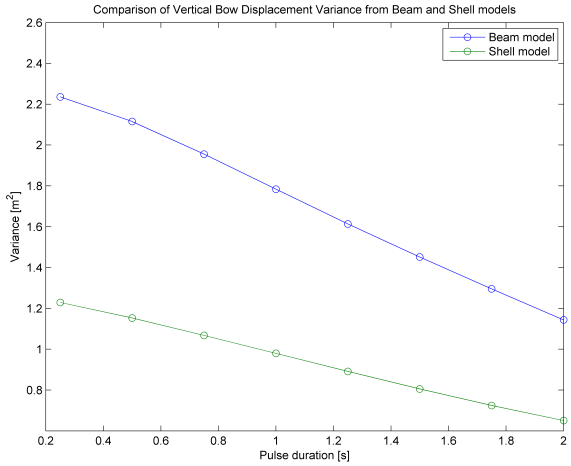

Figure 6.15: Comparison of vertical bow displacement variance predicted by beam and shell models

6.3 Parametric Study

In order to determine the sensitivity of the results to different parameter variations, a parametric study has been carried out using the simplified beam model. The study investigates variation of parameters related to both ice load representation and structural modelling, including different mass and damping models. Also, the results obtained using two different solution methods are compared.

6.3.1 Load Pulse Shape

Apart from varying the duration of the applied load pulse, which has been done in the main analyses, several different force-time histories have been investigated in order to determine their effect on the results. Figure 6.16 gives a graphical representation of the pulse shapes that have been included in the study.

All the triangular pulse shapes have the same impulse magnitude corresponding to the area below the force-time curve. The impulse magnitude of the *parabolic* pulse is approximately 33 % larger than that of the triangular pulses, and it is therefore assumed to give a somewhat larger response, which is consistent with the analytical results presented in figure 3.5. Further, the *left-skewed* and *right-skewed* pulse shapes have maximum values at 1/3 and 2/3 of the pulse duration, respectively.

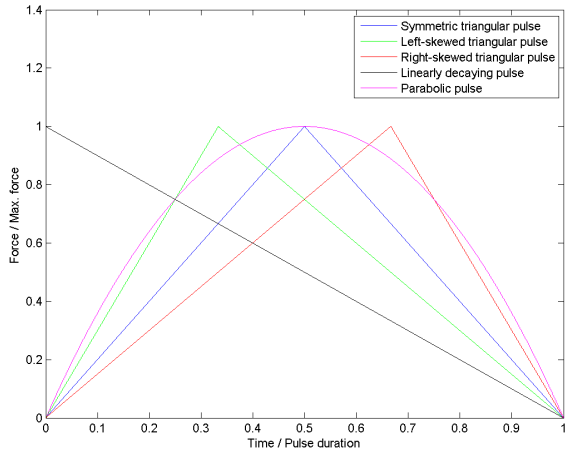

Figure 6.16: Different load pulse shapes applied in parametric study

Skewed pulse shapes

Figure 6.17 compares dynamic response from the two skewed pulse shapes with the symmetric triangular pulse. It is observed that there is virtually no difference between the three cases other than a minor phase shift to the left for the left-skewed pulse and to the right for the right-skewed pulse. The phase shift becomes larger in the respective direction for increasing pulse duration, as can be seen from the plots included in appendix C.

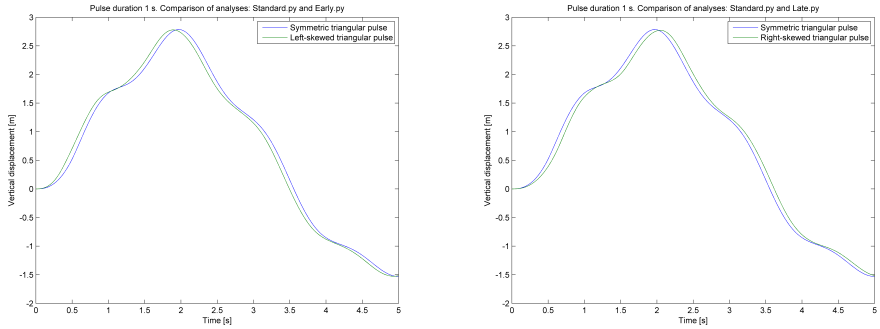

Figure 6.17: Comparison of response from left- and right-skewed pulse shapes with symmetric triangular pulse shape (1 s pulse)

Parabolic pulse shape

Dynamic response using the parabolic pulse shape is compared with the symmetric triangular pulse in figure 6.18. It can be seen that the response is very similar in the two cases. As expected, the response is larger for the parabolic pulse, but the difference is negligible for a pulse duration of 1 s. However, this difference increases for longer pulses, as can be seen from the plots given in appendix C.

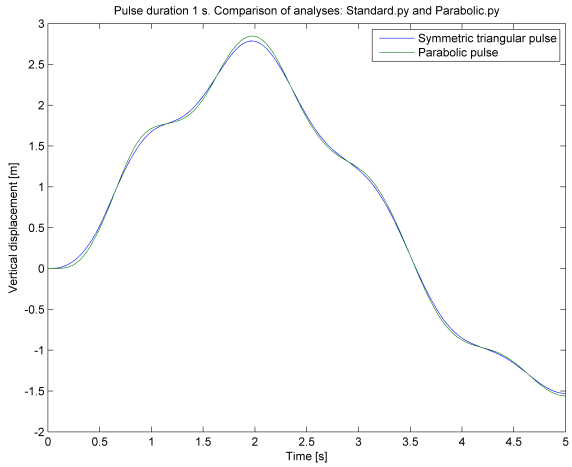

Figure 6.18: Comparison of response from parabolic and symmetric triangular pulse shapes (1 s pulse)

Linearly decaying pulse shape

Figure 6.19 gives a comparison of dynamic response using the linearly decaying pulse shape and the symmetric triangular pulse. The response from the decaying pulse is shifted towards the left compared with the symmetric pulse, which is to be expected due to the instantaneous application of the load during the first time increment. As the pulse duration is increased, the phase shift also increases in the same manner as for the left-skewed pulse. The shift is however larger for the decaying pulse, since the maximum force occurs earlier than for the left-skewed pulse shape. Similar plots for pulse durations in the range 0.25-2.0 s are included in appendix C.

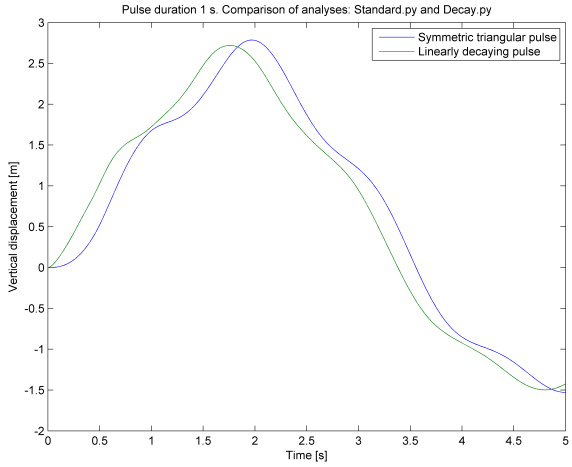

Figure 6.19: Comparison of response from linearly decaying and symmetric triangular pulse shapes (1 s pulse)

Effect of pulse shape

From the discussion given above, it can be concluded that the pulse shape is of minor importance for shorter pulses, in this case below approximately 1 s. However, as the duration of the load pulse is increased, the response becomes more dependent upon the shape. The largest difference is seen between the linearly decaying and the symmetric triangular pulses. There is however only a phase difference between the response histories, while the peak values are virtually identical within the investigated duration interval.

A difference in peak response can only be observed between the parabolic and symmetric triangular pulses. The impulse magnitude of the parabolic pulse is however approximately 33 % larger than that of the symmetric triangular pulse in the current analyses, thus explaining the difference in peak response.

6.3.2 Distribution of Mass

As previously discussed, the mass of the vessel has been modelled by use of an equivalent material density. For the simplified beam model, this corresponds to a uniform mass distribution along the vessel length. In order to investigate the importance of mass distribution, a *lumped* mass model has also been applied in which the mass of the vessel is assumed concentrated at each beam node.

The lumped mass model will approach the uniform mass distribution as the number of elements is increased. In the present analyses, 64 beam elements have been

applied along the vessel length, corresponding to a nodal spacing of approximately 1.6 m, meaning an equal spacing of concentrated masses.

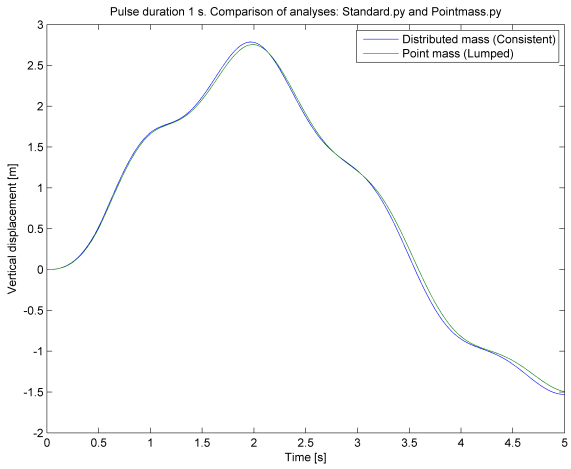

Figure 6.20: Comparison of response using different mass models (1 s pulse)

A comparison of dynamic response using the two mass models is given in figure 6.20 for a load pulse of duration 1 s. It is clearly seen that the difference between the two response histories is negligible. However, the difference increases for shorter pulse durations, which is the opposite conclusion as that regarding the pulse shape dependency. Similar plots are given in appendix C for the 0.25-2.0 s pulse duration interval.

6.3.3 Damping Model

In the main analyses, damping has been introduced at modal level by application of Rayleigh damping, assuming a critical damping ratio of 0.05 for the two- and three-node bending modes. According to figure 6.3, the critical damping ratio will be larger for all other modes, including the rigid body motions, which will have a damping ratio of approximately 0.18.

To assess the importance of damping, the Rayleigh model has been compared with results obtained using a constant critical damping ratio of 0.05 independent of modal frequencies. Since the total damping will be lower when applying a constant damping ratio, the maximum response is expected to be larger than when using the Rayleigh damping model.

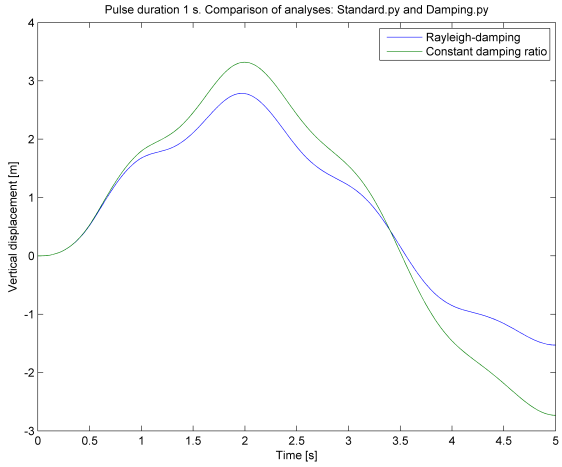

Figure 6.21: Comparison of response using different damping models (1 s pulse)

Dynamic response histories for the two damping models are given in figure 6.21 for a pulse duration of 1 s. It is seen that the difference in response magnitude is significant compared with the results obtained for other parameter variations. Since damping occurs as dissipation of energy over time, the difference in response will grow as the analysis time elapses. The difference seems to be independent of the pulse duration, as can be seen from the plots included in appendix C.

6.3.4 Solution Method

As previously discussed, modal superposition has been used as solution technique for the beam model, while direct implicit time integration was applied for the shell model. In order to examine the influence of solution method on the results, both aforementioned methods are applied for the beam model. Due to the relatively low complexity of the beam model, no major discrepancies are expected between results obtained using the two different solution methods.

Figure 6.22 gives a comparison of the dynamic response obtained by the two solution methods for a load pulse of 1 s. As expected, there is virtually no difference between the two response histories, suggesting that the choice of solution method is unimportant for analyses carried out with the beam model. Similar plots are given in appendix C for other pulse durations, showing no difference between the solution methods.

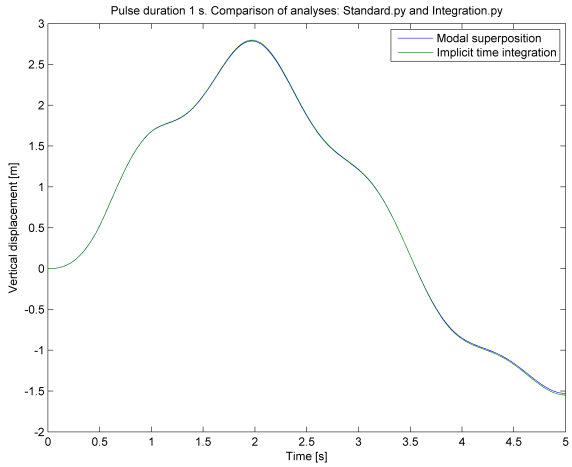

Figure 6.22: Comparison of response using different solution methods (1 s pulse)

Chapter 7

Comparison with Measurement Data

During the course of the ILM project, large amounts of measurement data have been collected during sea trials in ice-infested waters. The vessel KV Svalbard has been instrumented with different equipment, including strain gauges in the bow region and a *motion reference unit*, to record time series of local and global response.

Several earlier master's theses carried out at NTNU have dealt with measurement data from the ILM project, thereof [Børsheim, 2007] and [Espeland, 2008]. However, only strain measurements have been examined due to lack of global motion recordings during sea trials performed in 2006 and 2007. The data of interest for the current analyses are time series of global vertical motion in the bow region during ramming, which will be compared with corresponding results from FE models of KV Svalbard.

7.1 Configuration of MRU

The MRU on board KV Svalbard records displacements, velocities and accelerations for all rigid body degrees of freedom except roll angle. It is installed on a longitudinal bulkhead at 20500 ABL, 23.6 m astern of FP [Nyseth, 2010]. The origin of the coordinate system adapted by the MRU is defined at the centre of gravity of the vessel, which is shown in figure 7.1. Output data from the MRU is converted from raw binary format to ASCII using MATLAB-routines developed by DNV.

As previously discussed, the heave and pitch motions will be those of relevance during head-on ramming, and the vertical displacement in the bow will be a combi-

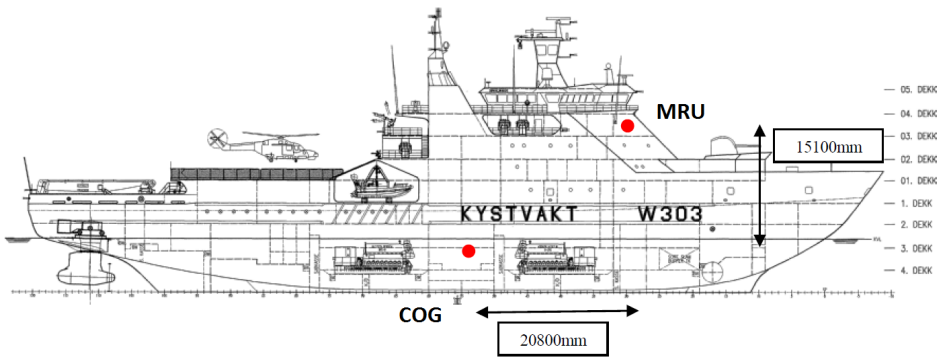

Figure 7.1: Location of COG and MRU on KV Svalbard [Nyseth, 2010]

nation of these two components. The total vertical displacement can be calculated using the following equation, assuming only rigid body motion [Faltinsen, 1990]:

$$S_3 = \eta_3 - X\eta_5 \tag{7.1}$$

The parameter X denotes the distance from COG to bow, while η_3 and η_5 express heave displacement and pitch angle, respectively. The pitch angle is defined positive when the bow moves downwards, thus explaining the negative sign occurring in equation (7.1).

7.2 Measurement Data

The measurement data to be analysed is taken from a KV Svalbard sea trial conducted on March 16, 2012 where response during ice ridge ramming was recorded. During a two-hour period of recording, one ridge impact was registered at 12:54 GMT. The ice ridge was located in the Greenland Sea between Greenland and Svalbard, as seen in figure 7.2.

The vertical bow displacement during the one-minute period 12:54-12:55 is shown in figure 7.3, where the first response peak after ridge impact is highlighted. As can be observed, the peak vertical displacement following the ridge impact is approximately 0.64 m. Ramming of the ridge was performed from open water, meaning there was no significant level ice in front of the ridge prior to impact. Maximum forward velocity immediately before impact was recorded by the vessel GPS system to be 4.4 m/s, which is above the minimum ramming speed of 2.0 m/s as defined in [DNV, 2011].

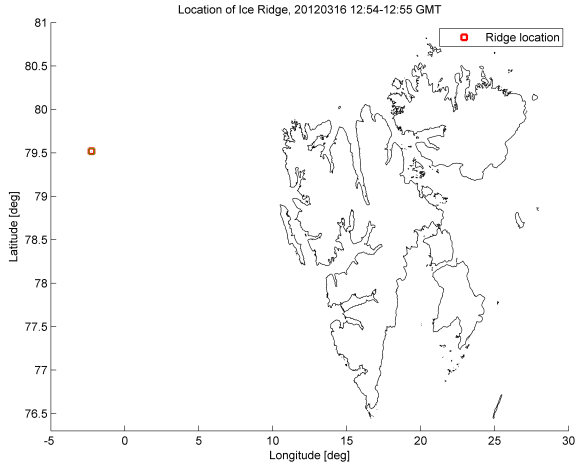

Figure 7.2: Location of ice ridge on March 16, 2012 at 12:54 GMT

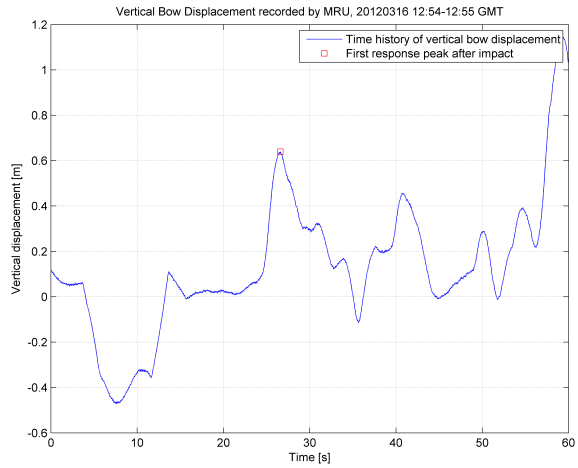

Figure 7.3: Measured vertical bow displacement on March 16, 2012 at 12:54-12:55 GMT

7.3 Comparison of Data and Analyses

From figure 7.3, it is apparent that the maximum measured vertical bow displacement is significantly smaller than the corresponding results obtained from FE analyses, which predicted lowest maximum response for the 2 s load pulse. It is therefore

natural to compare the measured response with results from the simplified beam model when subjected to a 2 s load pulse.

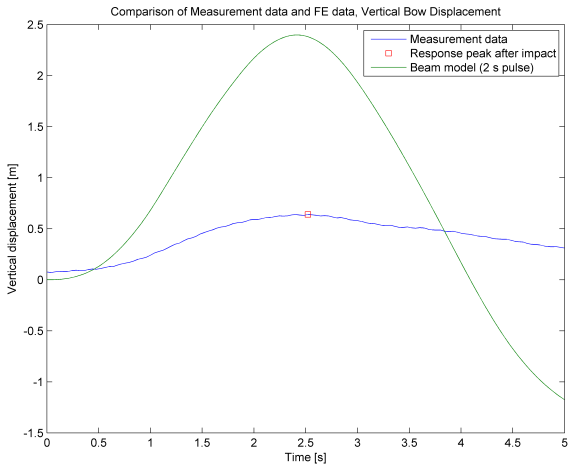

Figure 7.4: Comparison of vertical bow displacement from measurement data and original beam model

In figure 7.4, the measured response immediately following the initial ridge impact is compared with the response obtained from the simplified beam model using a symmetric triangular load pulse of 2 s duration. It is seen that the beam model peak response is close to 4 times larger than the measured peak response, which can be regarded as a significant difference. Further, the measured vertical displacement decays slowly after the peak value compared with the beam model response. This is most likely due to the bow sliding on top of the ridge, as investigated in [Riska, 1987].

In order to obtain closer agreement between measurement data and FE analysis results, an iterative procedure has been carried out where the load pulse shape and peak magnitude have been tuned such that the FE response approaches the measured response. The result of the iteration is displayed in figure 7.5, where the measured vertical bow displacement is compared with the corresponding response from the modified beam FE model. By visual observation, the two response histories are very similar.

To make a proper comparison between measured and calculated response, the maximum and mean displacements are calculated for the two response histories, along with the response variances. The maximum response of the modified beam FE model is virtually equal to the measured peak response, while very good agreement is obtained both for mean response and variance. The obtained values along with deviations between measured and calculated response are given in table 7.1.

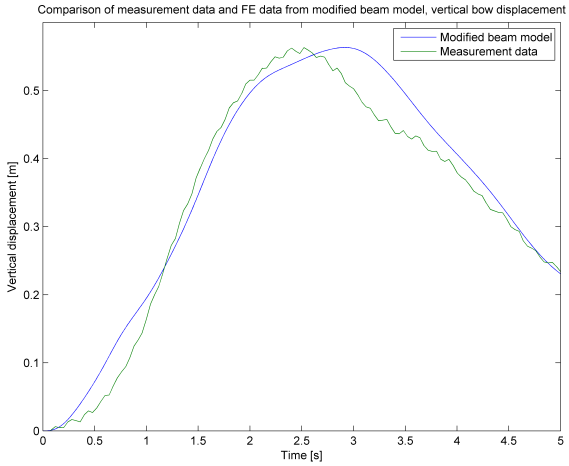

Figure 7.5: Comparison of vertical bow displacement from measurement data and modified beam model

The force-time history applied in the modified beam FE model is presented in figure 7.6. It is seen that the force is ramped to its maximum value during the first 0.2 s, and is further linearly reduced to 60 % of maximum value in the time interval 0.2-1.6 s. From 1.6-5.0 s, the force is kept constant at 60 % of maximum value.

Parameter	Measured data	FE data	Deviation
Maximum	0.5632 m	0.5633 m	0.0221 %
Mean	0.3388 m	0.3553 m	4.8637 %
Variance	0.0311 m^2	0.0299 m^2	-3.9090 %

Table 7.1: Comparison of statistical parameters from measurement data and modified beam model

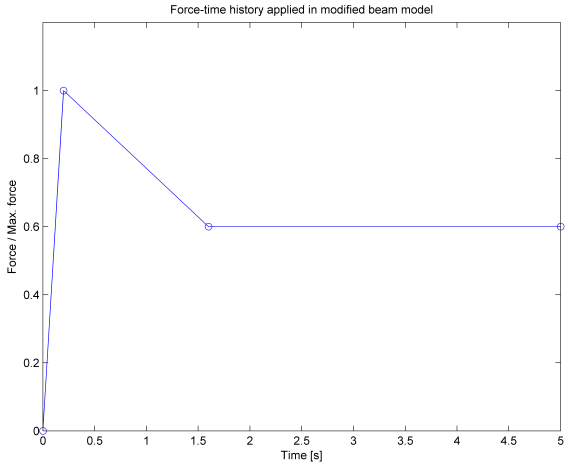

Figure 7.6: Modified force-time history

Not only the shape of the pulse has been modified, but also the maximum force, which was previously taken equal to 24.49 MN for the 1 s symmetric triangular pulse. In the modified beam FE model, the maximum force applied is only 7.88 % of the previous value, or 1.92 MN. This is significantly lower than what is regarded as the design ramming force in [DNV, 2011]. However, since only one ramming sequence has been analysed, it is not possible to determine whether the response is representative for other ramming sequences. It is further unknown whether the ice conditions faced during the sea trial were representative design conditions in terms of ice strength and other relevant parameters.

Chapter 8

Concluding Remarks

The main endeavour of this thesis work has been to study different aspects related to design of ice-going vessels. In particular, global vessel response during ramming impact between vessel and ice ridge has been focused on. The introductory part of the thesis presents some important aspects related to sea ice, including physical and mechanical properties, along with an overview of different types of ice features present in the Arctic region. A discussion related to important ship-ice interaction models for local hull pressure and global loading is also preformed.

A comparative study of design rules developed by DNV and IACS has been conducted, and important differences between the two separate rules have been identified. While DNV defines several different design load scenarios, IACS operates with a glancing impact load only. A general conclusion is that the DNV design rules are more specific in terms of governing design scenarios, while the IACS design rules are more universal when it comes to vessel type and prevailing ice conditions.

Two separate global FE models have been developed based on the coastguard vessel KV Svalbard, where dynamic and quasi-static response analyses have been carried out for ice ridge impact loading. The simplified beam model predicts overall larger maximum vertical bow displacement compared to the detailed shell model, but the difference decreases as the pulse duration of the applied loading is increased. Difference in response prediction is presumably caused by excitation of the beam model two-node bending mode for shorter load pulses.

Further, a linear relationship between dynamic load factor and pulse duration of the ice ramming load has been observed for both FE models. The DLF is seen to increase as the pulse duration is increased within the investigated range 0.25-2.0 s. Quasi-static response is overall larger than the dynamic response for both models due to short load pulse duration compared to natural heave period of the vessel.

A parametric study has been performed in order to investigate the importance of different pulse shapes, mass models, damping models and solution methods. It can

be concluded that the load pulse shape is of minor importance for dynamic response when the pulse duration is short. However, the pulse shape becomes increasingly important for longer load pulses within the investigated duration interval. An opposite trend can be observed for the difference in response using uniform and lumped mass models, where a negligible difference is seen for longer load pulses. The difference increases somewhat for shorter load pulses, but can be considered unimportant for dynamic response within the investigated duration interval.

The parametric study has shown that choice of damping model is of significant importance compared with other investigated parameters. Analyses using Rayleigh-damping produces overall lower response than the application of a constant critical damping ratio of 5 %, independent of load pulse duration. On the other hand, difference in results using modal superposition and implicit time integration is virtually non-existent, implying that choice of solution method is unimportant for analysis using the beam FE model.

In order to verify the applicability of the two models, full scale measurements of global motions from KV Svalbard during ice ridge impact have been analysed and compared with FE results. The difference between measured and calculated vertical bow displacement is significant, even when applying a load pulse of 2 s duration, which predicts lowest maximum response in FE analyses. An iterative procedure has been carried out with the intention of reproducing the measured response history using a modified beam FE model. By applying an irregular pulse shape with peak load corresponding to 7.88 % of the rule design load, the agreement between measured and calculated response is quite strong.

Chapter 9

Recommendations for Further Work

The FE models developed during the thesis work need further refinement, in particular the detailed shell model. In order to obtain a better representation of the global hull girder stiffness, longitudinal stringers and girders should be included in the model. It is believed that the absence of these structural components in the present shell model explains why excitation of the two-node bending mode only occurs for the simplified beam model.

Modelling of hydrodynamic forces such as added mass, damping and buoyancy has been done using simple analytical methods. Further refinement on this part should include a hydrodynamic analysis using software such as *Wadam*, which can produce numerical values for hydrodynamic forces that are far more accurate. An improvement with regards to the distribution of mass should also be addressed, in particular concerning proper modelling of topside weight.

The FE analyses carried out with the shell model only consist of a single load patch configuration. Further analyses should therefore include variation of load patch size, as well as load patch location in the bow region, in order to investigate the effect on predicted response. The applied pressure must be varied accordingly to ensure a constant resultant force.

In order to gain better understanding of global vessel response during ice ridge impact, further sea trials should be conducted including response measurements for a larger number of ramming sequences. The full scale measurement data analysed in this thesis only includes one ramming sequence, and it is therefore not possible to determine whether the measured peak response is representative for other ramming sequences. Ideally, extreme value statistics should be determined for peak response during ice ridge ramming, but such an effort would require an extensive sea trial scheme.

The procedure of reproducing the measured vertical bow displacement using the beam FE model has been carried out manually. In the event that response measurements from a larger number of ramming sequences are made available, the procedure could be automated using least-squares fitting or similar procedures.

Bibliography

[Bergan et al., 1983] Bergan, P. G., Larsen, P. K., and Mollestad, E. (1983). *Svingning av Konstruksjoner*. Tapir Forlag.

[Brodtkorb et al., 2000] Brodtkorb, P., Johannesson, P., Lindgren, G., Rychlik, I., Rydén, J., and Sjö, E. (2000). WAFO - a Matlab toolbox for the analysis of random waves and loads. In *Proc. 10'th Int. Offshore and Polar Eng. Conf., ISOPE, Seattle, USA*, volume 3, pages 343–350.

[Børsheim, 2007] Børsheim, L. (2007). Ship Hull Monitoring of Ice-Induced Stresses. Master's thesis, Norwegian University of Science and Technology.

[Chen et al., 1990] Chen, Y. K., Tunik, A. L., and Chen, A. P. Y. (1990). Global Ice Forces and Ship Response to Ice - Analysis of Ice Ramming Forces. *Ship Structure Committee*, SSC-342.

[Dassault Systemes, 2011] Dassault Systemes (2011). *Abaqus Analysis User's Manual*.

[DNV, 2011] DNV (2011). *Rules for Classification of Ships, Pt.5 Ch.1: Ships for Navigation in Ice*. Det Norske Veritas.

[Espeland, 2008] Espeland, Ø. (2008). Ice Action and Response Monitoring of Ships. Master's thesis, Norwegian University of Science and Technology.

[Faltinsen, 1990] Faltinsen, O. M. (1990). *Sea Loads on Ships and Offshore Structures*. Cambridge University Press, UK.

[Furnes, 2011] Furnes, G. (2011). *Lecture notes in Ice I*. NTNU.

[IACS, 2011] IACS (2011). *Requirements Concerning Polar Class*. International Association of Classification Societies.

[Kamarainen, 1993] Kamarainen, J. (1993). Studies in Ice Mechanics. *Helsinki University of Technology*.

[Korzhavin, 1971] Korzhavin, K. N. (1971). *Action of Ice on Engineering Structures*. US Army CRREL Translation TL260.

[Lainey and Tinawi, 1984] Lainey, K. and Tinawi, R. (1984). The Mechanical Properties of Sea Ice - a Compilation of Available Data. *Canadian Journal of Civil Engineering*, 11:119–127.

[Løset et al., 2006] Løset, S., Shkhinek, K. N., Gudmestad, O. T., and Høyland, K. V. (2006). *Actions from Ice on Arctic Offshore and Coastal Structures*. LAN.

[Nyseth, 2010] Nyseth, H. (2010). *KV Svalbard - ColdTech Project. Configuration of Motion Sensor MRU-H*. Det Norske Veritas.

[Popov et al., 1968] Popov, Y., Faddeev, O., Kheisin, D., and Yakovlev, A. (1968). *Strength of Ships Sailing in Ice*. US Army Foreign Science and Technology Centre, Technical Translation.

[Riska, 1987] Riska, K. (1987). *On the Mechanics of the Ramming Interaction Between a Ship and a Massive Ice Floe*. PhD thesis, Technical Research Centre of Finland.

[Riska, 2011] Riska, K. (2011). *Ship-Ice Interaction in Ship Design: Theory and Practice. Design of Ice Breaking Ships*. Lecture notes in Ice II, NTNU.

[Sanderson, 1988] Sanderson, T. J. O. (1988). *Ice Mechanics. Risk to Offshore Structures*. Graham and Troutman, London.

[Timco and Frederking, 1990] Timco, G. W. and Frederking, R. M. (1990). Compressive Strength of Sea Ice Sheets. *Journal for Cold Regions Science and Technology*, 17:227–240.

[Timco and O'Brien, 1994] Timco, G. W. and O'Brien, S. (1994). Flexural Strength Equation for Sea Ice. *Journal for Cold Regions Science and Technology*, 22:285–298.

[WMO, 1970] WMO (1970). *World Meteorological Organization Sea-Ice Nomenclature Vol. 1: Terminology and Codes*. World Meteorological Organization.

Appendix A

Determination of Waterplane Area

This appendix contains a description of how the waterplane area of the vessel has been calculated.

Determination of Waterplane Area

	Triangle 1	Trapezoid 1	Trapezoid 2	Rectangle 1	Trapezoid 3
The irregular geometry	4,93692	8,655123	8,970373	35,554383	9,206617
of the deck is split into	6,996207	8,00007	4	9,206617	10,846401
simple geometric		6,996207	8,655123		8,889239
shapes for which the	**17,2698571**	**62,6058678**	**35,250992**	**327,335587**	**98,1374553**
area can be calculated					
using Abaqus CAE. The	Trapezoid 4	Trapezoid 5	Trapezoid 6	Trapezoid 7	Triangle 2
area of each geometric	8,889239	7,759467	5,386489	3,837881	5,487297
shape is summed	8	8,090698	3,909302	1,080202	3,369977
together, giving the	7,759467	5,386489	3,837881	3,369977	
total area of the deck.	**66,594824**	**53,17998**	**18,030424**	**3,89297131**	**9,24603234**

Area of deck 5400 ABL	**1383,09**
Length	89,90
Breadth	18,41
Rectangular area	**1655,43**
Waterplane coeff.	**0,84**
Length in waterline	94,54
Breadth in waterline	18,56
Waterplane area	**1465,91**

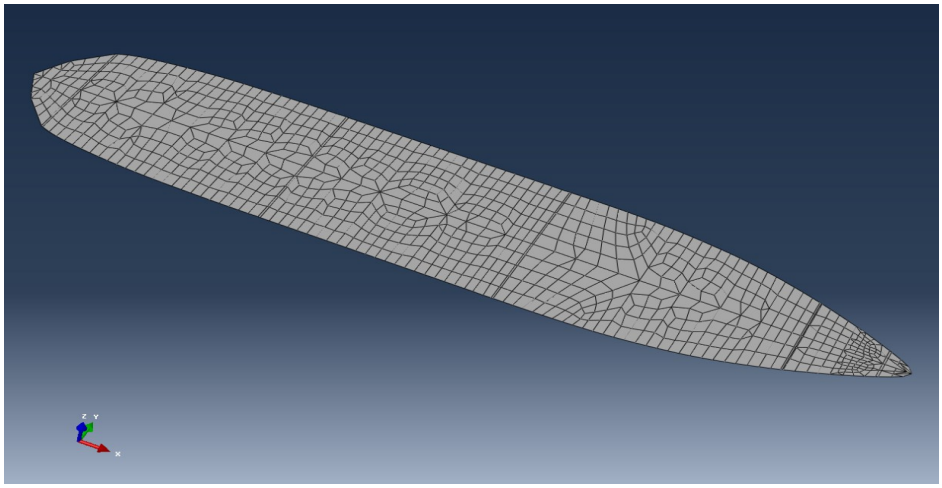

Appendix B

Comparison of FE Models

This appendix contains plots that compare the response obtained from the simplified beam and detailed shell FE models. The plots show vertical bow displacement for load pulse durations in the range 0.25-2.0 s.

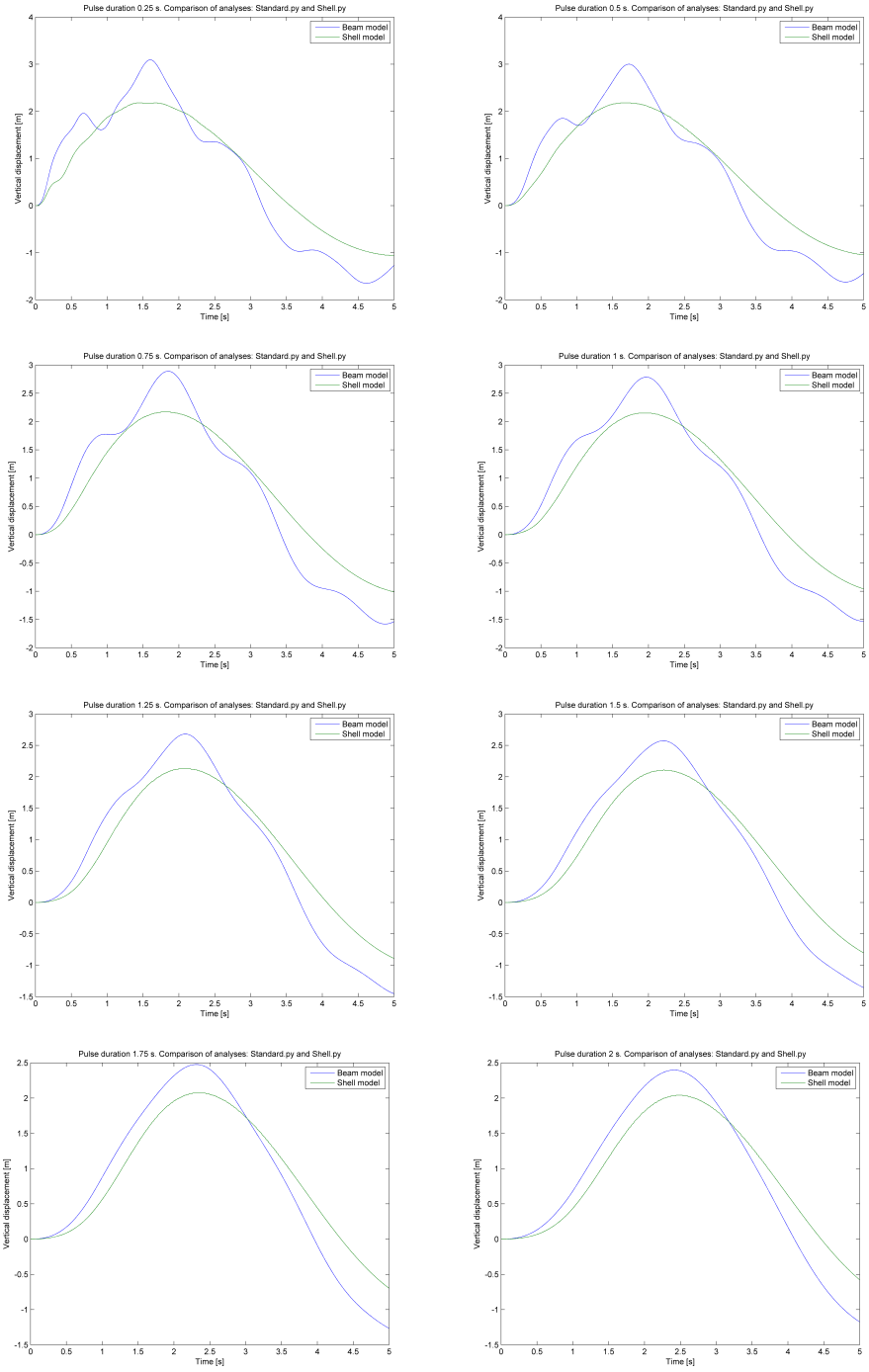

Figure B.1: Comparison of response predicted by beam and shell models

Appendix C

Parametric Study

This appendix contains results from the parametric study carried out by use of the simplified beam FE model. The plots show time series of vertical bow displacement for load pulse durations in the range 0.25-2.0 s.

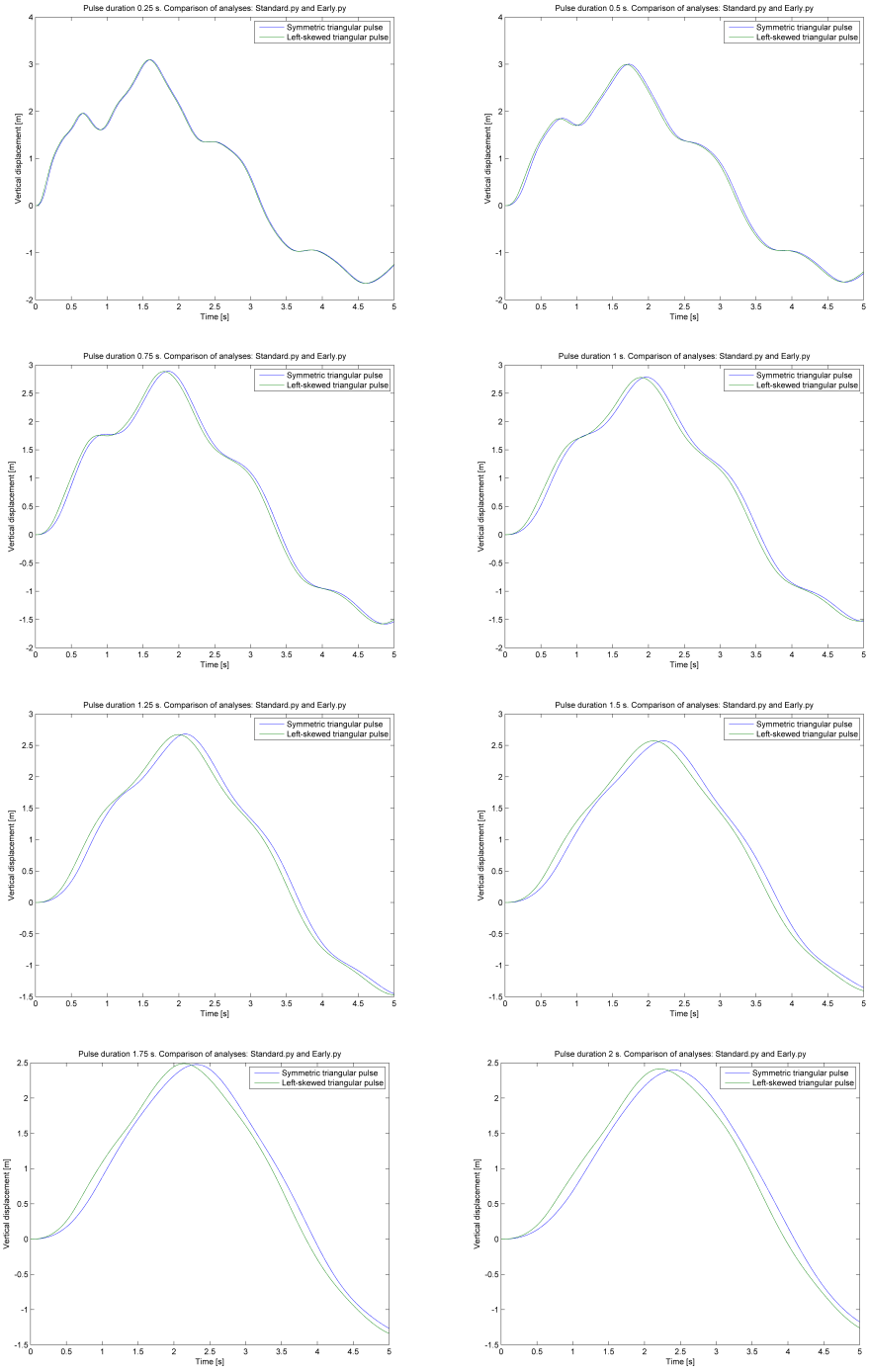

Figure C.1: Comparison of response using symmetric triangular and left-skewed pulse shapes

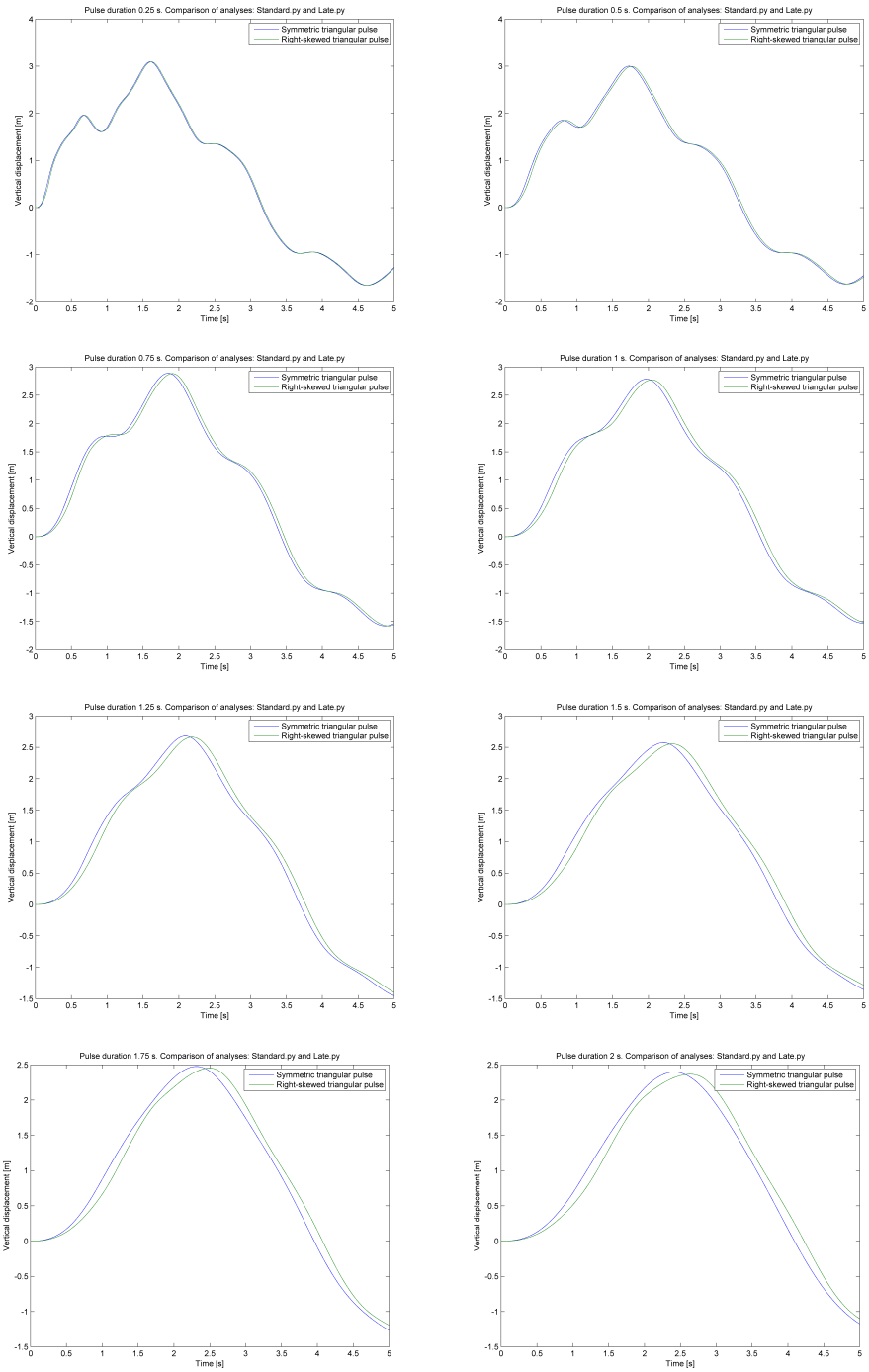

Figure C.2: Comparison of response using symmetric triangular and right-skewed pulse shapes

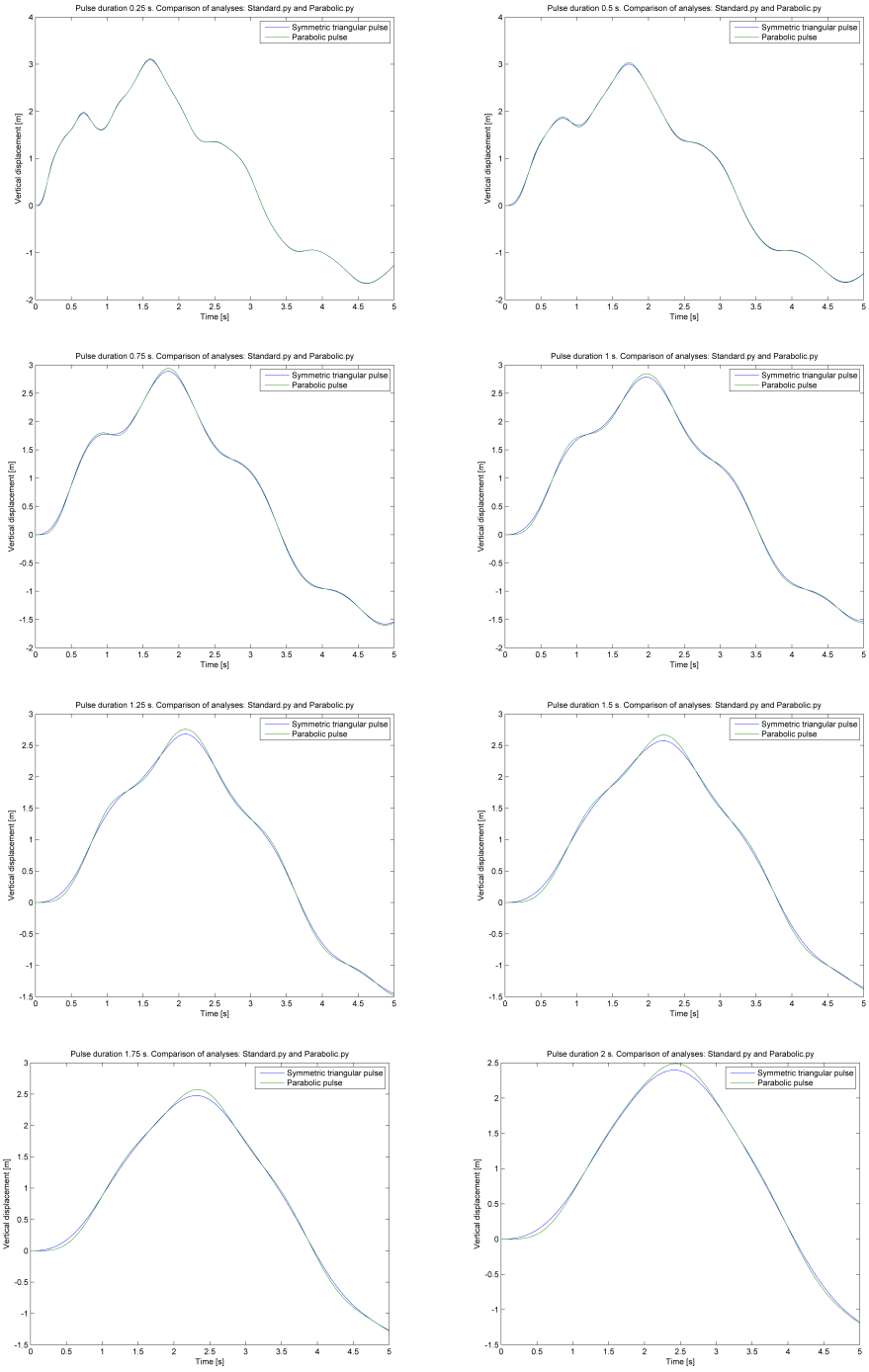

Figure C.3: Comparison of response using symmetric triangular and parabolic pulse shapes

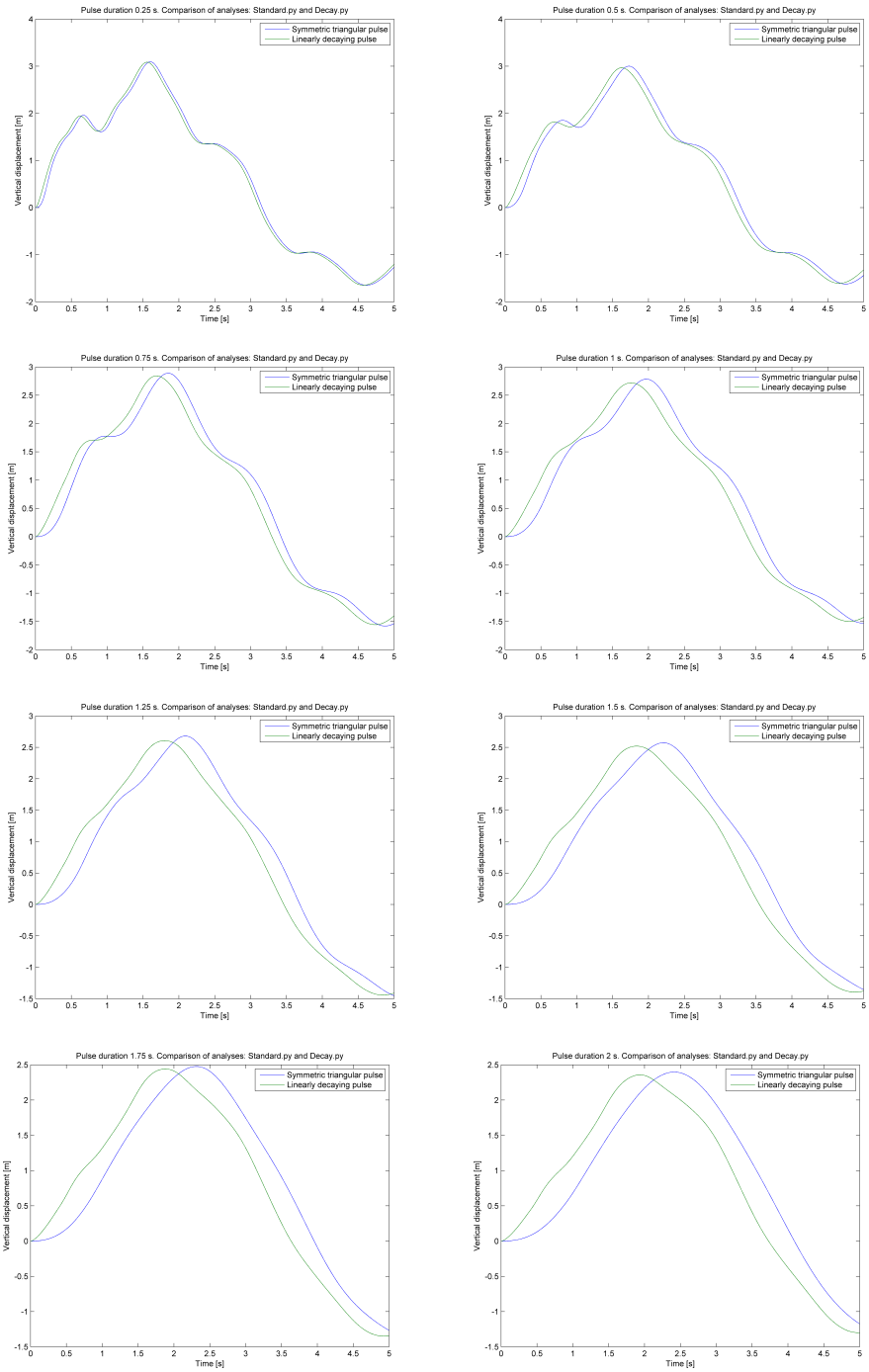

Figure C.4: Comparison of response using symmetric triangular and linearly decaying pulse shapes

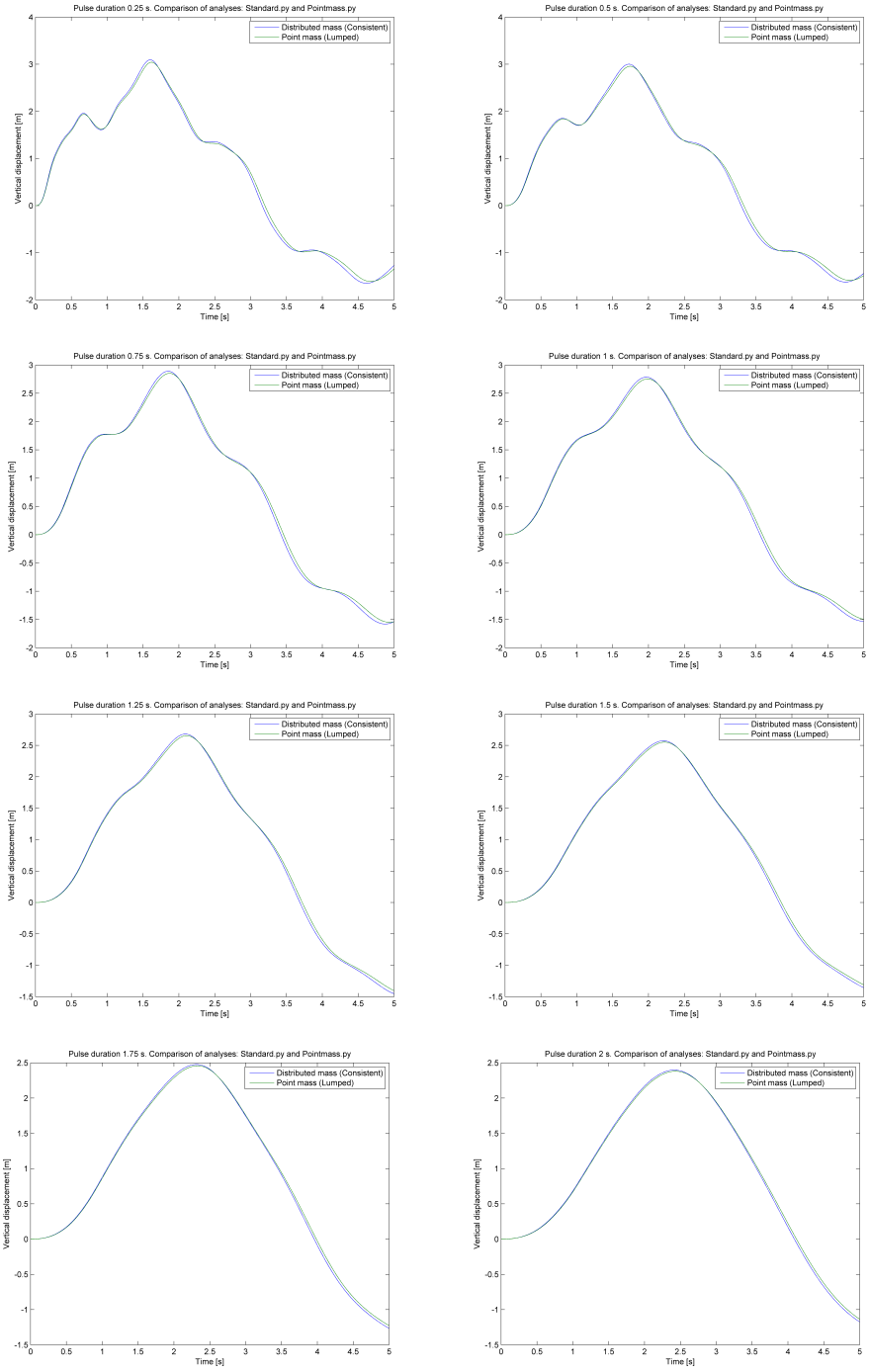

Figure C.5: Comparison of response using uniformly distributed and lumped mass models

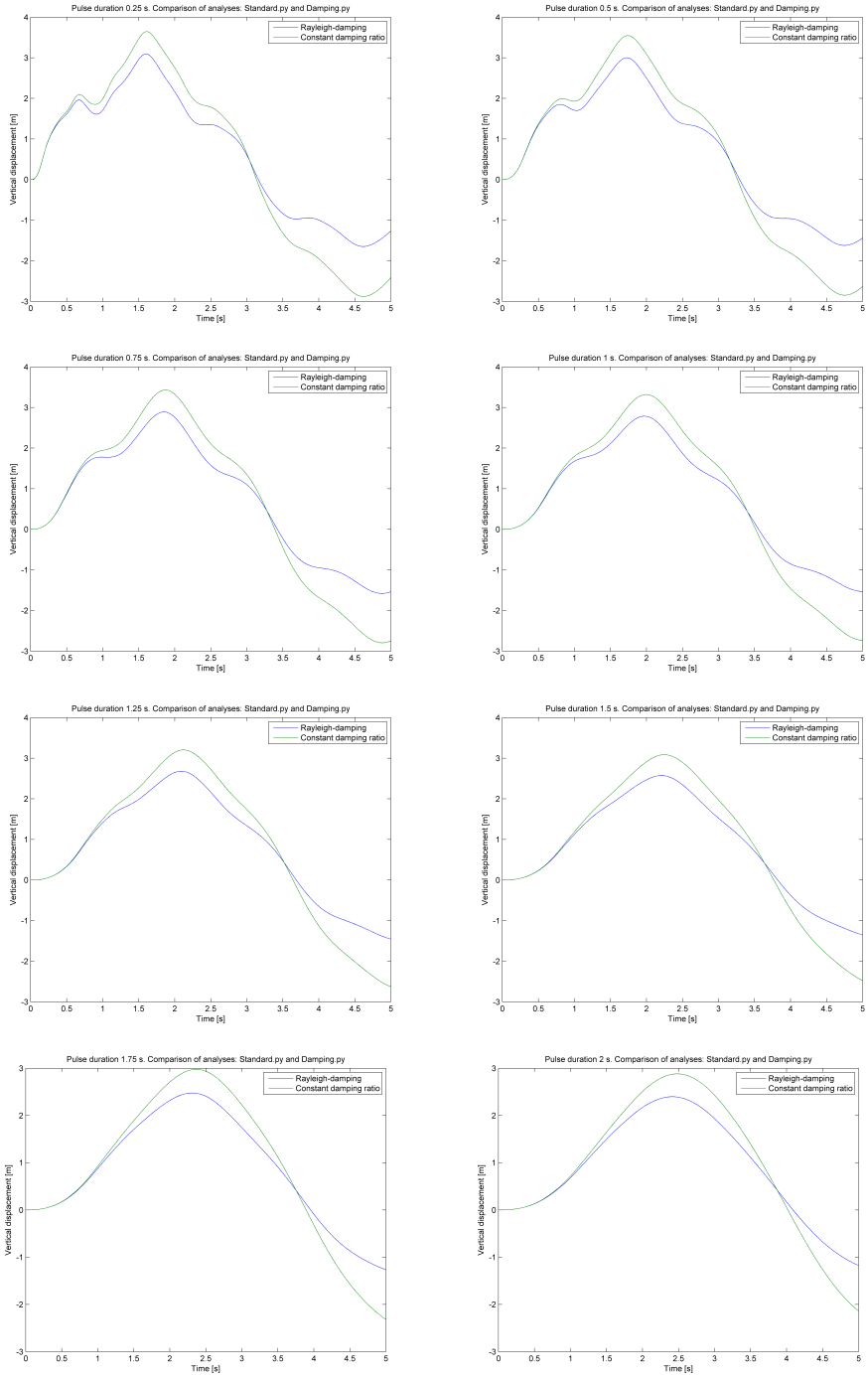

Figure C.6: Comparison of response using Rayleigh-damping and constant damping

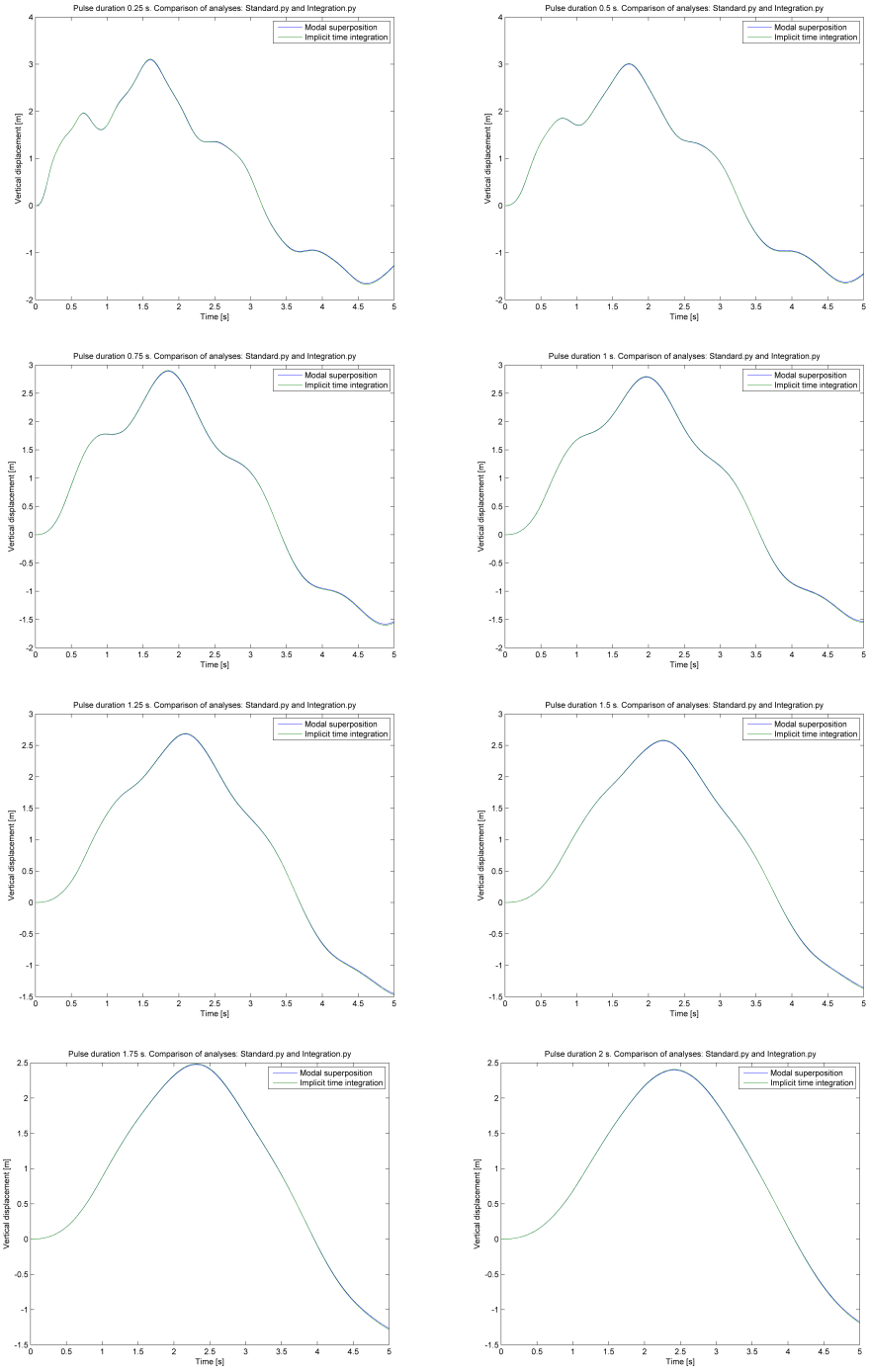

Figure C.7: Comparison of response using modal superposition and implicit time integration